

Resolving discharge parameters from atomic oxygen emission

Citation for published version (APA):

Viegas, P., Vialetto, L., van de Steeg, A. W., Wolf, A. J., Bongers, W. A., van Rooij, G. J., van de Sanden, M. C. M., Diomede, P., & Peeters, F. J. J. (2021). Resolving discharge parameters from atomic oxygen emission. *Plasma Sources Science & Technology*, 30(6), [065022]. <https://doi.org/10.1088/1361-6595/ac04bd>

Document status and date:

Published: 01/06/2021

DOI:

[10.1088/1361-6595/ac04bd](https://doi.org/10.1088/1361-6595/ac04bd)

Document Version:

Publisher's PDF, also known as Version of record

Document license:

Taverne

Please check the document version of this publication:

- A submitted manuscript is the version of the article upon submission and before peer-review. There can be important differences between the submitted version and the official published version of record. People interested in the research are advised to contact the author for the final version of the publication, or visit the DOI to the publisher's website.
- The final author version and the galley proof are versions of the publication after peer review.
- The final published version features the final layout of the paper including the volume, issue and page numbers.

[Link to publication](#)

General rights

Copyright and moral rights for the publications made accessible in the public portal are retained by the authors and/or other copyright owners and it is a condition of accessing publications that users recognise and abide by the legal requirements associated with these rights.

- Users may download and print one copy of any publication from the public portal for the purpose of private study or research.
- You may not further distribute the material or use it for any profit-making activity or commercial gain
- You may freely distribute the URL identifying the publication in the public portal.

If the publication is distributed under the terms of Article 25fa of the Dutch Copyright Act, indicated by the "Taverne" license above, please follow below link for the End User Agreement:

www.umlib.nl/taverne-license




Take down policy

If you believe that this document breaches copyright please contact us at:

repository@maastrichtuniversity.nl

providing details and we will investigate your claim.

Resolving discharge parameters from atomic oxygen emission

P Viegas^{1,4,*}, L Vialetto¹, A W van de Steeg¹, A J Wolf¹,
W A Bongers¹, G J van Rooij^{1,2,3}, M C M van de Sanden^{1,2},
P Diomede^{1,3} and F J J Peeters¹

¹ DIFFER—Dutch Institute for Fundamental Energy Research, 5612 AJ Eindhoven, The Netherlands

² Department of Applied Physics, Eindhoven University of Technology, PO Box 513, 5600 MB Eindhoven, The Netherlands

³ Faculty of Science and Engineering, Maastricht University, Zwingelput 4, ZW4, 6211 KH Maastricht, The Netherlands

E-mail: viegas@mail.muni.cz

Received 5 March 2021, revised 6 May 2021

Accepted for publication 25 May 2021

Published 25 June 2021



Abstract

A method is proposed to spatially resolve discharge parameters from experimental measurements of emission intensity and 1D numerical simulations including an O atom collisional-radiative model. The method can be used for different plasmas and conditions. Here, contracted microwave discharges for CO₂ conversion are studied at intermediate to high pressures (100–300 mbar). Radial profiles of electron density (n_e) are used as input in the model and corrected to successfully simulate the measured Gaussian profiles of emission intensity of the 777 nm transition (I_{777}). As a result, radially-resolved parameters inaccessible in experiments, such as n_e , power density (P_{abs}), electron temperature (T_e), electric field and reaction rates, are numerically-obtained for several conditions. n_e and P_{abs} approximately follow Gaussian profiles that are broader than that of I_{777} . For pressures below 150 mbar, the difference in full width at half maximum is typically a factor 1.6. This consists in a phenomenon of optical contraction, which is due to concave profiles of O molar fraction and T_e . The implications of the simulated profiles on the study of plasmas for CO₂ conversion are discussed and it is shown that these profiles allow to explain high reactor performances at low pressures.

Keywords: atomic oxygen kinetics, discharge spatial resolution, optical contraction, discharge contraction, CO₂ conversion

(Some figures may appear in colour only in the online journal)

1. Introduction

The understanding of low-temperature plasma physics and the optimisation of its applications is dependent on our knowledge of the spatial distributions of physical parameters in discharge reactors. Among those parameters, electron density (n_e), electron temperature (T_e), gas composition, gas temperature (T_g), reduced electric field (E/n_g), emission intensity

and power density (P_{abs}) are often some of the most important. In fact, the spatial distribution of discharge parameters has been vastly studied but is only well established for specific discharge configurations. A well known example is the case in low pressure discharge regimes controlled by free diffusion or by ambipolar diffusion, where the radial distribution of n_e in a long cylindrical discharge follows a paraboloidal or a zero-order Bessel function of the first kind with zero at the cylinder wall (Schottky 1924, Parker 1963, Ikegami 1968, Durandet *et al* 1989, Lieberman and Lichtenberg 2005, Fridman and Kennedy 2004, Moisan and Pelletier 2012). However,

* Author to whom any correspondences should be addressed.

⁴ Present address: Department of Physical Electronics at the Faculty of Science, Masaryk University, Kotlářská 267/2, 611 37 Brno, Czech Republic.

charged-particle balance in intermediate (a few to hundreds of mbar) to high pressure discharges relies on molecular ion recombination, and thus the Bessel profile cannot be assumed for cylindrical discharges in those conditions.

In several numerical and experimental works on glow and microwave (MW) discharges with atomic and molecular gases, n_e and emission intensity have been shown to have Bessel radial profiles at low pressures and currents when the discharge is diffuse, but significantly different, seemingly Gaussian profiles, at higher pressures or currents when the discharge contracts (Petrov and Ferreira 1999, Martinez *et al* 2004, Kabouzi *et al* 2007, Dyatko *et al* 2008, Golubovskii *et al* 2011, Shneider *et al* 2014, Golubovskii *et al* 2017, Ridenti *et al* 2018, Zhong *et al* 2019). In particular, in the work of Dyatko *et al* (2008) with a 1D-radial model describing an argon glow discharge at intermediate pressure, the ratio between the peak and the average electron densities has been calculated to change from 2.3 for a Bessel profile to 720 for a highly contracted discharge. Then, in Carbone *et al* (2012), radially-resolved n_e measurements through Thomson scattering in an MW argon plasma at intermediate pressure have been fitted with a Bessel function for which the boundary radius R defined by $n_e(R) = 0$ is a free parameter that decreases with pressure. Furthermore, in the 1D models in Gregório *et al* (2010, 2012) of argon MW microplasmas at atmospheric pressure, n_e contracts to a concave shape that is neither Gaussian nor Bessel. On the contrary, in the 2D numerical work in Baeva *et al* (2018) in an argon plasma torch at atmospheric pressure, the radial profile of n_e presented is rather flat.

Radiative emission takes place naturally in reactive plasmas, and therefore emission intensity can be an easily accessible source of spatially-resolved information in the discharge. Nevertheless, in contracted conditions, the n_e profile can be spatially more extended than the optical appearance of the plasma suggests. Indeed, experimental radial distributions of line emission have been reported to be more compressed than that of n_e (obtained from the Bremsstrahlung continuum) in neon in Golubovskii *et al* (2011) and in helium in Golubovskii *et al* (2020). This effect has been called optical contraction and has been attributed in Golubovskii *et al* (2011) to the influence of electron–electron collisions on the electron energy distribution function (EEDF), which enhances electron-impact excitation and ionisation reactions in the centre of the discharge. However, in Golubovskii *et al* (2020), this effect seems to be due to the low values of E/n_g in the radial edges, as E/n_g is theoretically estimated to have a significantly concave distribution in that work. The concave shape of E/n_g is in agreement with the experimental measurements and simulations of concave profiles of T_e in Kabouzi *et al* (2007), Gregório *et al* (2010), Golubovskii *et al* (2011), Gregório *et al* (2012), Golubovskii *et al* (2017), Ridenti *et al* (2018), Zhong *et al* (2019). In fact, the simulations in Ridenti *et al* (2018) have shown that T_e in Thomson scattering measurements, such as those in van Gessel *et al* (2012), Carbone *et al* (2012), has a convex radial profile due to the Maxwellian assumption of this diagnostic, while T_e obtained from the calculated EEDF (2/3 of mean electron energy) actually has a concave radial profile, as does E/n_g . Conversely, the T_e and E/n_g radial profiles obtained in

the 1D and 2D simulations in Martinez *et al* (2004), Jimenez-Diaz *et al* (2012), Georgieva *et al* (2017), Baeva *et al* (2018) have been reported as approximately radially homogeneous. We can conclude that the relationships between the spatial profiles of different discharge parameters so far are not completely understood and cannot be generalised.

In this work, we address the spatial distribution of discharge parameters in MW CO₂ plasma reactors. These are intended to convert greenhouse gas CO₂ into carbon-neutral fuels or useful chemicals (Goede *et al* 2014, Guerra *et al* 2017, Snoeckx and Bogaerts 2017, Vermeiren and Bogaerts 2020). Spatial distributions in these discharges are particularly interesting, as the discharge radius has been shown to have a strong correlation with reactor performance, with the best conversion and energy efficiencies having been obtained when the core of the discharge has a radially-contracted structure (Fridman 2008, van Rooij *et al* 2015, den Harder *et al* 2017, Bongers *et al* 2017). In particular, the relationship between the spatial distribution of P_{abs} and the reactor performance has been highlighted in van den Bekerom *et al* (2019).

Recent studies have addressed the contraction dynamics and the radial structure of MW discharges for CO₂ conversion (Wolf *et al* 2019, Groen *et al* 2019, Wolf *et al* 2020a, 2020b, Viegas *et al* 2020, D'Isa *et al* 2020). The contraction of a vortex-stabilised CO₂ MW plasma has been characterised in Wolf *et al* (2019) in relation to its dielectric properties. Then, in Wolf *et al* (2020b), two distinct contracted discharge modes have been identified and described at pressures above 85 mbar: a low-confinement L-mode at lower pressures and at temperatures between 3000 and 5000 K and a high-confinement H-mode at higher pressures and at temperatures above 5500 K. The works in Viegas *et al* (2020) and Wolf *et al* (2020a) have investigated the contracted modes numerically. The distinct changes in spatial profiles of n_e and P_{abs} with discharge modes have been shown to be important to obtain accurate descriptions of the reactivity within the plasma, that determines the spatial structure of the plasma itself (Viegas *et al* 2020), as well as of the follow-up reactions of plasma products in its periphery, that influence the reactor performance (Wolf *et al* 2020a). Despite the importance of accurately determining these spatial profiles, discharge parameters are difficult to measure with mm resolution in CO₂ MW plasmas and are often based on the spatial distribution of parameters that are easier to obtain experimentally, such as the radiative emission intensity. As such, the works on CO₂ discharge contraction so far have relied on unverified simplifying assumptions on the spatial profiles of discharge parameters, such as n_e , P_{abs} and E/n_g . To self-consistently describe the relationships between these parameters and improve profile determination, it is very relevant to assess the assumptions used so far.

In this work, numerical simulations are used to determine spatially-resolved discharge parameters in a CO₂ MW discharge from the experimentally measured intensity distribution of the 777 nm spectral line emission of atomic oxygen: O(3p ⁵P) → O(3s ⁵S⁰) (I_{777}). This study requires a collisional-radiative model (CRM) of O atom kinetics. That type of description has been developed and used in works such as

Dagdikian *et al* (1988), Stancu *et al* (2016), Caplinger and Perram (2020), Fiebrandt *et al* (2020). In particular, in Fiebrandt *et al* (2020) a CRM has been developed to calculate excited state densities of atomic oxygen in zero dimensions in low pressure plasmas with varying Ar/O₂ mixtures. That work has highlighted the influence of radiative cascading between excited states and of radiation self-absorption. Moreover, in Caplinger and Perram (2020) a CRM focussed on the 777 nm/844 nm line ratio of atomic oxygen has been developed in zero dimensions to study oxygen plasmas at different pressures and with different dissociation degrees (ratio between O and O₂). The results of that CRM have been compared with those of more commonly-used models, such as the extended corona model. The relevance of stepwise excitation and cascade emission has been put forward in Caplinger and Perram (2020). Both of these recent works have discussed the choice and use of kinetic data in their CRMs.

This paper employs for the first time a CRM for atomic oxygen developed in the context of reactive CO₂ mixtures at intermediate to high pressures (100–300 mbar). We use it in 1D to radially resolve n_e , T_e , E/n_g and P_{abs} in contracted MW discharges for CO₂ conversion. In section 2, the experimental set-up is presented, along with the plasma conditions and the measurements undertaken. The set of hypotheses taken in the interpretation of experiments to relate the experimentally-measured Gaussian profiles $I_{777}(r)$ to the other discharge parameters is also explained. Then, the 1D-radial model developed in this work is explained in section 3, including the CRM for atomic oxygen. The simulation results are presented in section 4 for the different sets of conditions presented in section 2. First, an $n_e(r)$ profile calculated directly from experimental data is used as input in the simulations, in order to illustrate the shortcomings of some of the hypotheses taken. The dependence of $n_e(r)$ on $I_{777}(r)$, and vice-versa, is obtained and explained from the simulations, and leads to correcting the hypotheses considered so far and the assumptions for $n_e(r)$. The simulations show that the corrected assumptions are consistent with the measurements, and thus provide radially-resolved discharge parameters. Finally, the implications of these findings on the study of MW discharges for CO₂ conversion are demonstrated and discussed, along with the possibilities to apply this correction procedure to relate discharge parameters in different plasmas.

2. Experimental set-up, hypotheses and conditions

2.1. Experimental set-up and hypotheses on plasma parameters

The discharges studied in this work are obtained experimentally in a vortex-stabilised MW reactor. This configuration has been used in several works on plasma-driven CO₂ conversion (Butylkin *et al* 1981, Fridman 2008, Bongers *et al* 2017). The set-up is presented in figure 1 and described in more detail in Wolf *et al* (2019). It consists of a 2.45 GHz MW source, a rectangular waveguide field applicator and a three-stub tuner for impedance matching. The electromagnetic

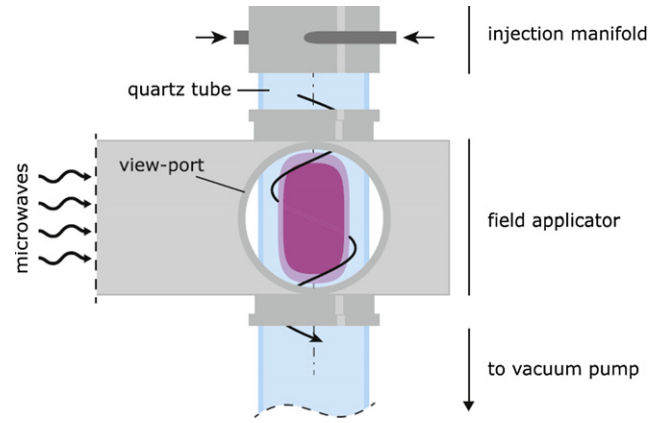


Figure 1. Illustration of the experimental setup, including the main plasma reactor components. Reproduced from [Wolf *et al* [2020b]]. © IOP Publishing Ltd. All rights reserved.

(EM) field is continuously coupled to a CO₂ gas flow, which is contained in a quartz tube of inner radius $R_{\text{tube}} = 13.5$ mm. The wave electric field is directed parallel to the discharge tube (transverse-electric (TE₁₀) single mode standing wave). The plasma is stabilised in the centre of the tube by means of a vortex flow, achieved by tangential gas injection, to prevent plasma-induced wall damage, as in Fleisch *et al* (2007). The discharge characteristics and the related performance of CO₂ conversion to CO in this reactor have been studied in detail in recent years in Wolf *et al* (2019, 2020b), Pietanza *et al* (2020), Wolf *et al* (2020a), Viegas *et al* (2020).

In Wolf *et al* (2019), the intensity distribution of the 777 nm spectral line emission of atomic oxygen ($\text{O}(3p^5P) \rightarrow \text{O}(3s^5S^0)$) has been measured to have a Gaussian radial profile $I_{777}(r)$ with full width at half maximum (FWHM) Λ_{777} and characteristic width (or standard deviation) $\sigma_{777} = \Lambda_{777} / (2\sqrt{2} \ln(2))$, that are invariant under an Abel transform:

$$I_{777}(r) = I_{777}(0) \exp\left(-\frac{1}{2} \frac{r^2}{\sigma_{777}^2}\right). \quad (1)$$

It is assumed in Wolf *et al* (2019) that $n_e(r)$ also follows a Gaussian radial profile, with peak n_{e0} , and is proportional to $I_{777}(r)$, with a proportionality parameter s , such that:

$$n_e(r) = n_{e0} \exp\left(-\frac{1}{2} \frac{r^2}{(\sqrt{s}\sigma_{777})^2}\right), \quad 1 \leq s \leq 2. \quad (2)$$

That assumption is based on the following hypotheses:

- (1) The upper state of the 777 nm emission, $\text{O}(3p^5P)$, of density $n_{\text{O}(3p^5P)}$, is produced mostly by electron-impact excitation of the atomic oxygen ground-state $\text{O}(2p^4^3P)$, of density $n_{\text{O}(2p^4^3P)}$, with rate coefficient $k_{\text{exc}}(T_e)$. $\text{O}(3p^5P)$ is mostly destroyed by radiative emission with coefficient τ_{rad}^{-1} and quenching by any neutral species (with gas density n_g) with coefficient k_Q . The radiation balance is then expressed as:

$$I_{777} = \tau_{\text{rad}}^{-1} n_{\text{O}(3p^5P)} \simeq \tau_{\text{rad}}^{-1} \frac{n_e n_{\text{O}(2p^4^3P)} k_{\text{exc}}(T_e)}{\tau_{\text{rad}}^{-1} + n_g k_Q}. \quad (3)$$

- (2) τ_{rad}^{-1} and k_Q are radially homogeneous, and $n_g k_Q > \tau_{\text{rad}}^{-1}$. Thus:

$$I_{777} \propto n_e x_O k_{\text{exc}}(T_e), \quad (4)$$

where $x_O = n_{\text{O}(2p^4 \ ^3p)}/n_g$.

- (3) E/n_g and T_e are radially homogeneous in the plasma region, and so is $k_{\text{exc}}(T_e)$.
- (4) x_O is defined by heavy-particle thermal reactions that are independent of n_e , and by electron-impact reactions with rates proportional to n_e . It is assumed that:

$$I_{777} \propto n_e^s, \quad 1 \leq s \leq 2. \quad (5)$$

The line-integrated electron density at the axial centre of the discharge ($n_{e\Lambda}$) has been measured in Wolf *et al* (2019), and thus the peak of n_e and the plasma diameter Λ_{n_e} (FWHM of the $n_e(r)$ profile) have been calculated according to the assumption in equation (2) as function of s :

$$n_{e0} = n_{e\Lambda} / \sqrt{2\pi(\sqrt{s}\sigma_{777})^2} \quad (6)$$

$$\Lambda_{n_e} = \sqrt{s}\Lambda_{777}. \quad (7)$$

Using these hypotheses, in Wolf *et al* (2019) the radius of the discharge column and the skin-depth of wave absorption have been found to have approximately the same value, for $1 \leq s \leq 2$. Then, in the subsequent studies of this discharge (Groen *et al* 2019, Wolf *et al* 2020b, Pietanza *et al* 2020, Wolf *et al* 2020a, Viegas *et al* 2020), as well as in the investigation of a similar CO₂ MW discharge (D'Isa *et al* 2020), the assumption in equation (2) has been used, with additional hypotheses:

- (5) x_O is defined by thermal chemistry and the radial gradient of gas temperature is lower than the one of n_e . Hence, x_O is radially homogeneous in the plasma region, and therefore:

$$s = 1; \quad n_e(r) = n_{e0} \exp\left(-\frac{1}{2} \frac{r^2}{\sigma_{777}^2}\right). \quad (8)$$

- (6) As the temperature, composition, E/n_g , T_e and electron collision frequency ν_c are considered radially homogeneous, the MW absorbed power density (P_{abs}) is assumed to have the same radial profile as n_e (Wolf *et al* 2020b):

$$P_{\text{abs}}(r) = P_{\text{abs}0} \exp\left(-\frac{1}{2} \frac{r^2}{\sigma_{777}^2}\right), \quad (9)$$

where $P_{\text{abs}0}$ is obtained by dividing the total input power by the normalised volume integral of the emission intensity.

2.2. Experimental conditions

In this paper, we use the model described in section 3 to evaluate the hypotheses listed in section 2.1 and to spatially resolve discharge parameters. Here we describe the different sets of experimental conditions considered as input in the model.

2.2.1. Condition A: low-confinement discharge. Firstly, a discharge in low-confinement mode, according to the definition in Wolf *et al* (2020b), is studied. This is a well characterised

discharge, which is contracted but with Λ_{777} close to half the tube diameter. It has been obtained at 110 mbar with a fixed steady-state input power of 950 W and a flow rate of 9 slm. The Gaussian-shaped emission intensity of the 777 nm line (following equation (1)) has a radial FWHM $\Lambda_{777} = 5.88$ mm and an axial FWHM $L_{777} = 21.40$ mm. The line-integrated electron density $n_{e\Lambda}$ has been measured through 140 GHz MW interferometry and the profile $n_e(r)$ has been assumed according to equations (6)–(8). The relative uncertainty in the measurement of $n_{e\Lambda}$ is of the order of 100% for pressures below 110 mbar and then decreases with pressure, reaching values of the order of 10% for pressures above 200 mbar (Wolf *et al* 2019, Viegas *et al* 2020). This diagnostic considers the plasma as an infinite homogeneous slab, which applies when the plasma size is large compared to the diagnostic beam dimensions. Since this approximation collapses under the narrow plasma conditions considered in this work, a correction factor is applied which accounts for the partial pass-through of the diagnostic beam through the plasma medium. This correction has not been considered in previous works (Wolf *et al* 2019, Groen *et al* 2019, Viegas *et al* 2020), which might lead to an underestimation of n_e in those works. The partial pass-through effect is accounted for by applying a correction factor α , whose calculation is further described in Mousavi *et al* (2021), such that:

$$n_{e\Lambda, \text{corrected}} = n_{e\Lambda, \text{measured}} \times \alpha. \quad (10)$$

The correction factor α is inversely proportional to the interferometry frequency and to Λ_{777} . In the current case, $\alpha = 1.32$ and the corrected $n_{e0} = 9.11 \times 10^{18} \text{ m}^{-3}$. The rotational temperature (taken as the same as the translational temperature T_g) and the densities of the main species in the plasma reactor (CO₂, CO, O₂ and O) are measured locally at the axial position of the centre of the waveguide with 1 mm radial resolution through spontaneous rotational Raman scattering. This diagnostic has been used to measure temperature in van den Bekerom *et al* (2019, 2020), van de Steeg *et al* (2020) and is further explained in van de Steeg *et al* (2021). As pointed out in our previous works assessing measurements and simulations of the main neutral species densities (Wolf *et al* 2020a, Viegas *et al* 2020, van de Steeg *et al* 2021), their value and spatial distribution are determined mostly by thermally-driven neutral chemistry and by fast transport processes. The data taken as input in the model are presented in figure 2. On the left side of the figure, the assumed profile $n_e(r)$ and the measured profile $T_g(r)$, and on the right side, the measured molar fractions of the main species.

2.2.2. Condition B: high-confinement discharge. The main characteristics of the studied discharges are defined by their confinement degree, which is largely dependent on input power and pressure (Wolf *et al* 2020b). As such, it is important to evaluate discharge parameters also in high-confinement mode. A flow rate of 12 slm is used, and a high-confinement discharge is obtained at 150 mbar with an input MW power of 860 W. T_g and composition are measured through Raman scattering, $n_{e\Lambda}$ is measured through 140 GHz interferometry and $n_e(r)$ is assumed through equation (8) after considering

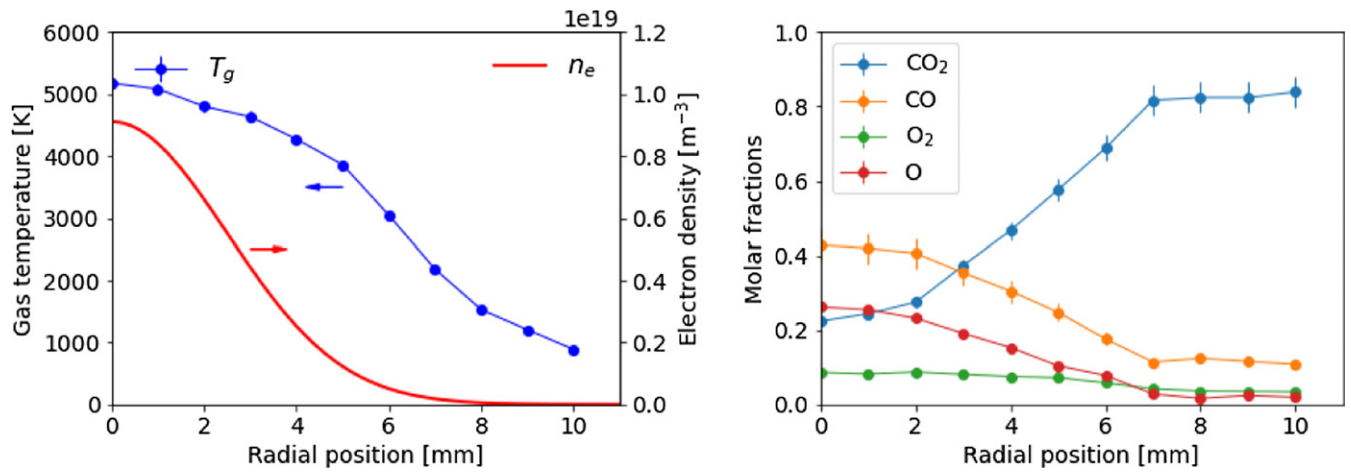


Figure 2. Radial profiles of experimental input parameters in condition A (950 W, 9 slm and 110 mbar). On the left, the assumed $n_e(r)$ and the measured $T_g(r)$. On the right, the measured molar fractions of CO_2 , CO , O_2 and O .

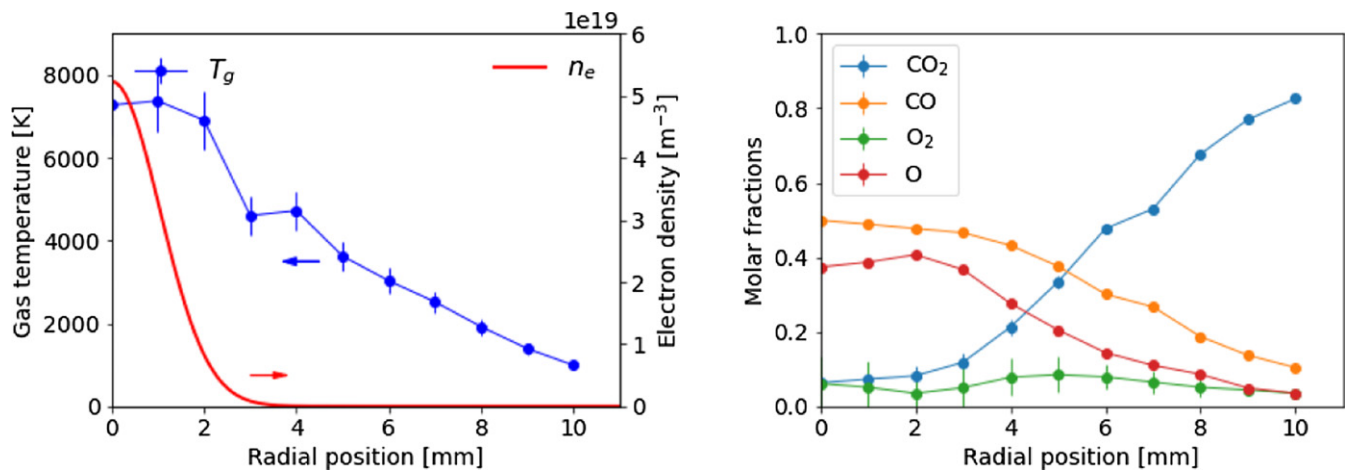


Figure 3. Radial profiles of experimental input parameters in condition B (860 W, 12 slm and 150 mbar). On the left, the assumed $n_e(r)$ and the measured $T_g(r)$. On the right, the measured molar fractions of CO_2 , CO , O_2 and O .

the correction factor α , as for condition A. The length L_{777} is 26.71 mm, the diameter Λ_{777} is 2.46 mm, below half of that of condition A, and the correction factor α is 2.69. $n_e(r)$ and $T_g(r)$ are represented on the left side of figure 3. The measured composition is shown on the right side of the same figure. The $n_e(r)$ and $T_g(r)$ profiles clearly have sharper gradients than in condition A and, as a result of the higher temperature, the CO and O molar fractions are higher and have broader profiles than in condition A.

2.2.3. Set of conditions C: input from flow modelling. In some high-confinement conditions, emission from C_2 is present in the plasma (although C_2 remains a minor constituent), which severely cripples the Raman scattering diagnostic. Therefore, it is relevant to study spatial profiles of discharge parameters in cases where neutral composition is known from simulation results, which also allows wider parameter scans. Unlike the case in conditions A and B, in the set of conditions C we take the radial distributions of T_g and neutral composition from the simulation results of the 2D model in Wolf *et al* (2020a), at the axial position of maximum temperature. In that work, the

peak gas temperature in the centre of the discharge has been taken as input from Doppler broadening measurements of the 777 nm atomic oxygen line emission (Wolf *et al* 2019). We study 7 discharge conditions in different confinement modes by changing only pressure. They are obtained with 1400 W input power and 18 slm flow rate and the pressure is increased from 108 mbar to 296 mbar. These conditions are described in Wolf *et al* (2019) and in Viegas *et al* (2020). However, the plasma dimensions considered here have been found as in Wolf *et al* (2020a), in a slightly different way than in the previous works. $n_e(r)$ is obtained from equation (8), with $n_{e\Lambda}$ measured from 168 GHz interferometry. Although n_{e0} is displayed in Wolf *et al* (2019) and in Viegas *et al* (2020), the correction factor α is not taken into account in the values in those works. For the sake of brevity, the radial profiles of n_e , T_g and composition are not represented here, but $T_g(r)$ and the molar fraction $x_{\text{O}}(r)$ are shown later in figure 13. Moreover, some of the main plasma parameters are listed in table 1. It can be noticed from Λ_{777} in table 1 that the confinement degree of these discharges (except at 108 mbar) stands between the ones of conditions A

Table 1. Experimental input parameters in the set of conditions C: pressure, length, diameter, n_e correction factor, corrected n_e peak and maximum of T_g .

p (mbar)	L_{777} (mm)	Λ_{777} (mm)	α	n_{e0} (10^{18} m^{-3})	$T_{g,\text{max}}$ (K)
108	12.1	6.44	1.09	1.61	4927
121	15.4	4.77	1.25	8.24	5562
141	18.9	3.97	1.40	24.62	6082
161	22.5	3.68	1.47	26.75	6220
209	34.4	3.64	1.48	53.58	6119
249	34.6	3.50	1.53	71.30	6064
296	57.5	3.56	1.51	98.45	6007

Table 2. List of species considered in the model, along with the internal energies of O excited states (Laher and Gilmore 1990, Kramida *et al* 2020).

Main neutral species	$\text{CO}_2, \text{CO}, \text{O}_2, \text{O}(2p^4^3\text{P}), \text{C}$
Charged species	$e, \text{O}^-, \text{CO}_2^+, \text{CO}^+, \text{O}_2^+, \text{O}^+, \text{C}^+$
Metastable states	$\text{O}(2p^4^1\text{D})$ (1.97 eV), $\text{O}(2p^4^1\text{S})$ (4.19 eV) $\text{O}(3s^5\text{S}^0)$ (9.15 eV), $\text{O}(3s^3\text{S}^0)$ (9.52 eV)
Radiative states	$\text{O}(3p^5\text{P})$ (10.74 eV), $\text{O}(3p^3\text{P})$ (10.99 eV) $\text{O}(3d^5\text{D}^0)$ (12.08 eV), $\text{O}(3d^3\text{D}^0)$ (12.09 eV)

and B. Furthermore, that is also the case for $T_{g,\text{max}}$ and, as such, the degree and extension of dissociation in these plasmas are also in between those of condition A (figure 2) and those of condition B (figure 3).

3. Numerical model

3.1. 1D-radial plasma fluid model

Resolving discharge parameters in space requires at least a one-dimensional (1D) description of the CO_2 conversion MW plasma. In this work, we have developed and used an in-house 1D-radial fluid model addressing the plasma at the core axial position, i.e. the position of the centre of the waveguide. The species in table 2 are considered.

The model consists in solving for every species k the steady-state mass balance equations of the form:

$$\begin{aligned} \nabla \cdot \Gamma_{\mathbf{k}} &= \frac{1}{r} \frac{d}{dr} \left(-r D_k \frac{d}{dr} [y_k \rho] \right) + \left(\frac{\Gamma_{\text{out},k}}{L} - \frac{\Gamma_{\text{in},k}}{L} \right)_z \\ &= m_k \left(\sum_j S_{j,k} - \sum_i L_{i,k} \right), \end{aligned} \quad (11)$$

where r is the radial coordinate, y_k is the mass fraction of species k and ρ is the total mass density of the mixture ($\rho = \sum_k m_k n_k = \sum_k y_k \rho$). $\Gamma_{\mathbf{k}}$, D_k , n_k and m_k are, respectively, the flux of mass density, the mass diffusion coefficient, the number density and the particle mass of species k . $S_{j,k}$ and $L_{i,k}$ are, respectively, the chemistry source and loss terms associated to reactions j and i acting on species k . The reactor under study is characterized by vortex-stabilization, a recirculation zone, turbulent transport and, therefore, complex flow patterns. As such, the local transport is largely unknown and

in this model, motivated by the work in Wolf *et al* (2020a), we describe it as being mostly determined by laminar and turbulent mass diffusion. The model therefore consists mostly of a reaction–diffusion description. An axial convective transport term is included as in Wolf *et al* (2020a), Viegas *et al* (2020), in the form of $\left(\frac{\Gamma_{\text{out},k}}{L} - \frac{\Gamma_{\text{in},k}}{L} \right)_z$, where L is the plasma length taken from the emission intensity as $L = L_{777}$, $\Gamma_{\text{in},k}$ is the flux of CO_2 entering the plasma length, and $\Gamma_{\text{out},k}$ is the flux of every product exiting the plasma. These fluxes are calculated from the conservation of mass flow rate as:

$$\Gamma_{k,z}(r) = m_k n_k(r) v_z(r) \quad (12)$$

$$v_z(r) = \frac{\dot{m}}{\rho(r)A} \quad (13)$$

where $v_z(r)$ is the axial convective velocity at position r , \dot{m} is the input mass flow rate of CO_2 at room-temperature and at reactor pressure and A is the tube cross section $A = \pi(13.5 \text{ mm})^2$.

As the electric field associated to the MW propagation in transverse-electric mode in the experiments is not axisymmetric, this model does not include the simulation of electric field through Maxwell's equations. Instead, an electron density profile $n_{e,\text{IN}}(r)$ (considering equation (2) dependent on s) is assumed and E/n_g at each position r is self-consistently calculated by iterating this parameter until the electron density $n_e(r)$ matches $n_{e,\text{IN}}(r)$. $n_e(r)$ is obtained from the ion densities through a quasi-neutrality assumption. As such, only the electric field magnitude is considered, and not its direction, which leads us to neglecting electric drift and charge separation. The convergence criteria of the simulation are twofold. One criterion consists in matching $n_e(r)$ with $n_{e,\text{IN}}(r)$ within 1%, for every position where $n_{e,\text{IN}}(r) > 7 \times 10^{16} \text{ m}^{-3}$. We should notice that this tolerance is lower than the experimental uncertainty. For positions with lower electron density, $n_e(r)$ is not required to match $n_{e,\text{IN}}(r)$ and the reduced electric field E/n_g is assumed to be 1 Td, taken as a minimum value in the simulations. The other convergence criterion consists in imposing a solver tolerance for residuals of mass fractions of 10^{-6} . The model takes quantities from experiments presented in section 2 as input: p , L_{777} , flow rate, $n_{e,\text{IN}}(r)$ (where $n_{e,\Lambda}$ and Λ_{777} are included), $T_g(r)$ and radially-resolved composition. Concerning $T_g(r)$ and composition, a linear interpolation is taken in between measured points. For $r > 10 \text{ mm}$, where measurements are not available, the values at $r = 10 \text{ mm}$ are assumed. The influence of experimental uncertainties associated to quantities used as input in the model, such as n_e and T_g , in plasma chemistry simulation results has been put forward in Viegas *et al* (2020). As the electron density is obtained from quasi-neutrality, the simulations solve equation (11) for a total of 15 species: C, O^- , CO_2^+ , CO^+ , O_2^+ , O^+ , C^+ and the metastable and radiative excited states of atomic oxygen. The mass fraction of ground-state $\text{O}(2p^4^3\text{P})$ is obtained from subtracting the mass fractions of the O excited states $\text{O}(i)$ to the input one of O as $y_{\text{O}(2p^4^3\text{P})} = y_{\text{O}} - \sum_i y_{\text{O}(i)}$. The measured molar fractions of CO_2 , CO, O_2 and O are given as input to the model and allow to calculate $\rho(r)$ according to the ideal

gas law. Then, the mass fractions of these species are slightly adjusted during the simulations in order to preserve the ideal gas law. The reactions corresponding to the chemistry source terms $S_{k,j}$ are described in section 3.2.

As radial transport in the reactor under study is largely unknown, we describe it for the 15 species in the same way as in Wolf *et al* (2020a), where simulation results have found good experimental agreement. Radial transport is described in this model through laminar and turbulent Fickian mass diffusion, with the diffusion coefficient of each species k defined as the sum of a laminar coefficient $D_{L,k}$ and an effective turbulent coefficient D_T :

$$D_k(r) = D_{L,k}(r) + D_T(r). \quad (14)$$

The turbulent diffusion coefficient is taken from Wolf *et al* (2020a), where it is defined independently of the mixture as:

$$D_T(r) = \frac{\nu_T(r)}{Sc_T}, \quad (15)$$

with constant turbulent Schmidt number $Sc_T = 0.71$ (Yimer *et al* 2002), and turbulent viscosity $\nu_T(r)$. The same formulation has been adopted in Synek *et al* (2015). In Wolf *et al* (2020a), in agreement with computational fluid dynamics simulations of the vortex flow including a plasma heat source, it is stated that the radial variation in $\nu_T(r)$ can be approximated by a quadratic function of r :

$$\nu_T(r) = \nu_{T,\text{peak}} \cdot \left(1 - \frac{r^2}{R_{\text{tube}}^2}\right). \quad (16)$$

Then, the value on the axis $\nu_{T,\text{peak}}$ has been found in Wolf *et al* (2020a) for several conditions of pressure and flow and for an input power of 1 kW, as the value that best allows to retrieve the experimental peak of T_g , obtained from Doppler broadening measurements of the 777 nm atomic oxygen line emission (Wolf *et al* 2019). An improvement is made with respect to the case in Wolf *et al* (2020a), as the laminar diffusion coefficient in this work is obtained for each species k through a mixture-averaged multicomponent approach, as in Hirschfelder and Curtiss (1949), Giovangigli (1990), Synek *et al* (2015):

$$D_{L,k}(r) = \frac{1 - y_k}{\sum_{l \neq k} \frac{x_l}{D_{k,l}}}, \quad (17)$$

where x_l is the molar fraction of species l and $D_{k,l}$ is the binary diffusion coefficient of the (l, k) pair of species. The binary diffusion coefficients have been computed for all neutral–neutral, ion–neutral and electron–neutral interactions from Chapman–Enskog theory (Capitelli *et al* 2013), using the collision integrals in Laricchiuta *et al* (2009). In the conditions of this work, in the plasma core region, for ions and neutrals, $D_{L,k}$ and D_T are of the same order of magnitude, around $10^{-2} \text{ m}^2 \text{ s}^{-1}$.

The MW absorbed power density $P_{\text{abs}}(r)$ is calculated as an output through the steady-state electron energy balance equation (Alves *et al* 2018):

$$\begin{aligned} P_{\text{abs}}(r) = & \left(\frac{P_{\text{el}}}{n_g}(r) + \frac{P_{\text{inel}}}{n_g}(r) + \frac{P_{\text{growth}}}{n_g}(r) \right) n_g(r) n_e(r) \\ & + \frac{n_e(r) \epsilon(r) v_z(r)}{L} \\ & + \frac{d}{dr} \left(-\frac{5}{3} D_e(r) \frac{d}{dr} [n_e(r) \epsilon(r)] \right), \end{aligned} \quad (18)$$

where P_{el} , P_{inel} and P_{growth} are the components of power lost by electrons through elastic, conservative inelastic and non-conservative inelastic collisions, respectively, calculated from the solver for electron kinetics and dependent on E/n_g and gas mixture. ϵ is the mean electron energy also calculated from the electron kinetics solver and D_e is the electron diffusion coefficient, calculated from equations (14)–(17). We should notice that the formulation used for the diffusive term in equation (18) is an approximation based on the assumption of a Maxwellian electron velocity distribution function and an energy-independent momentum-transfer collision frequency (Alves *et al* 2018). However, in the studied conditions, the transport terms (mostly diffusive) in equation (18) have a weight of the order of only 2% on the calculation of P_{abs} , that is mostly defined by the collisional electron losses. Hence, formulating the transport terms differently would have a negligible effect on $P_{\text{abs}}(r)$.

The electron kinetics solver is the Monte Carlo flux (MCF) code developed and described in Vialletto *et al* (2019, 2020), based on the method introduced in Schaefer and Hui (1990). It is used in this model to calculate the power loss terms and the electron mean energy in equation (18) and the electron-impact rate coefficients that take part in the source term calculations. The MCF code can simulate electrons in any arbitrary gas mixture, including any population of excited states for atoms/molecules. Moreover, it is consistent with the cross sections set for electron impact used in this work. The importance of these considerations for the calculation of rate coefficients has been demonstrated in Viegas *et al* (2020), Vialletto *et al* (2020). The MCF solution is coupled to the 1D-radial model in a similar way as it was coupled to the zero-dimensional model in Viegas *et al* (2020). In 11 equally-spaced positions in the domain, the MCF solution is obtained for 21 values of reduced electric field linearly spaced between 1 and 200 Td. Then, the solution is interpolated in space. As such, the calculated electron parameters are functions of the local E/n_g and of position. The electron kinetics calculations take as input parameters the gas pressure and the frequency of the field, as well as the local gas temperature and composition, consistently with the plasma model and the experimental conditions reported in section 2. The vibrational states of molecules are taken into account in electron collisions by assuming that they are populated according to a Boltzmann distribution at T_g , as in Viegas *et al* (2020). The importance of considering these populations for electron kinetics in CO_2 has been demonstrated for example in Grofulović *et al* (2016), Vialletto *et al* (2020), Silva *et al* (2020). The MCF solutions are first obtained for the input molar fractions of the main species CO_2 , CO , O_2 and O . Then, after the plasma simulation converges, the MCF solutions are updated and the plasma simulation is run again.

Table 3. List of atomic oxygen reactions: electron-impact excitation, deexcitation, ionisation and dissociation; electron–ion recombination; and radiative emission taking self-absorption into account. $O(i)$ and $O(j)$ represent any state of atomic oxygen listed in table 2, except when a note is added. The units of rate coefficients for radiative emission are s^{-1} , and for two-body reactions are $cm^3 s^{-1}$. E/n_g is the reduced electric field; r is the radial position, corresponding to a local gas mixture and temperature; and T_e is the electron temperature in eV.^{a,b}

Nbr	Reaction	Rate coefficient	References
O1	$e + O(i) \leftrightarrow e + O(j)$	$k(E/n_g, r)$	[1, 2, 3]
O2	$e + O(i) \rightarrow e + O^+$	$k(E/n_g, r)$	[1]
O3	$e + CO_2 \rightarrow e + CO + O(2p^4 \ ^1S)$	$k(E/n_g, r)$	[4]
O4	$e + CO \rightarrow e + C + O(2p^4 \ ^1S)$	$k(E/n_g, r)$	[4]
O5	$e + O_2 \rightarrow e + O(2p^4 \ ^3P) + O(i)^a$	$k(E/n_g, r)$	[2, 4–8]
O6	$e + O_2^+ \rightarrow O(2p^4 \ ^3P) + O(2p^4 \ ^3P)$	$5.17 \times 10^{-9} \times T_e^{-1}$	[9, 10]
O7	$e + O_2^+ \rightarrow O(2p^4 \ ^3P) + O(2p^4 \ ^1D)$	$1.51 \times 10^{-8} \times T_e^{-0.7}$	[9, 11]
R1	$O(3p \ ^5P) \rightarrow O(3s \ ^5S^0) (777 \text{ nm})$	τ_{rad1}^{-1}	[12–14]
R2	$O(3p \ ^3P) \rightarrow O(3s \ ^3S^0) (845 \text{ nm})$	τ_{rad2}^{-1}	[12–14]
R3	$O(3d \ ^5D^0) \rightarrow O(3p \ ^5P) (926 \text{ nm})$	τ_{rad3}^{-1}	[12–14]
R4	$O(3d \ ^3D^0) \rightarrow O(3p \ ^3P) (1128 \text{ nm})$	τ_{rad4}^{-1}	[12–14]
R5	$O(3d \ ^3D^0) \rightarrow O(2p^4 \ ^3P) (102 \text{ nm})$	τ_{rad5}^{-1}	[12–14]
R6	$O(3s \ ^3S^0) \rightarrow O(2p^4 \ ^3P) (130 \text{ nm})$	τ_{rad6}^{-1}	[12–14]

^aReferences: [1] = Laher and Gilmore (1990); [2] = Alves *et al* (2016); [3] = Barklem (2007); [4] = McConkey *et al* (2008); [5] = Erdman and Zipf (1987); [6] = Lawrence (1970); [7] = Itikawa (2009); [8] = Kanik *et al* (2003); [9] = Annušová *et al* (2018); [10] = Kossyi *et al* (1992); [11] = Eliasson and Kogelschatz (1986); [12] = NIST database, Kramida *et al* (2020); [13] = Fiebrandt *et al* (2020); [14] = Mewe (1967).

^bNotes on the states considered: a— $O(2p^4 \ ^1D)$, $O(2p^4 \ ^1S)$, $O(3s \ ^5S^0)$, $O(3s \ ^3S^0)$, $O(3p \ ^5P)$ and $O(3p \ ^3P)$.

The update takes into account the calculated densities of C and of the atomic oxygen excited states, that have influence on the EEDF through both superelastic and stepwise inelastic collisions. As the densities of these species are much lower than those of the main species (whose fractions are fixed) and have only a minor effect on the EEDF, the MCF solutions are updated only once. In this way, electron kinetics is coupled self-consistently with plasma simulations.

The equations in this model are solved with a finite volume discretisation in a uniform grid, where diffusive mass fluxes are discretised using a central difference scheme. These are solved using the tridiagonal matrix algorithm for matrix inversion. Homogeneous Neumann boundary conditions for the radial diffusive fluxes are taken at $r = 0$ and at the tube wall. In this work the 13.5 mm radial domain is divided into 41 cells of 0.33 mm size each. The numerical solution is obtained in a single central processing unit with a calculation time ranging typically between 1 and 7 days. One simulation has been performed with 81 cells of 0.17 mm size each and has produced a relative difference in results up to 5% and an increase in calculation time of a factor 5.5, with respect to the same case with 41 cells. The calculation time is mostly due to the MCF calculations taking approximately 11 h (1 h per position) and to the very high number of iterations required to fulfil the convergence criteria, which is usually between 2 million and 20 million. On the one hand, the high number of iterations is justified by the use of a small under-relaxation factor of 10^{-5} , necessary for the resolution of the very stiff non-linear system of equations imposed by the complex chemistry in plasmas (Patankar 1980). On the other hand, we should notice that it is very computationally expensive to simultaneously match n_e with $n_{e,IN}$ in the whole domain, but it is of fundamental impor-

tance for the current study of spatial resolution of discharge parameters.

3.2. O atom collisional-radiative model in CO₂ conversion plasma

In this section, the reaction scheme used in the model is presented. The reactions considered in Viegas *et al* (2020) are adopted in this work. These include reactions for neutral thermal chemistry based on the GRI-MECH 3.0 database (Smith *et al* 2018) and for charged particle kinetics based on the reaction schemes of Koelman *et al* (2017), Kozák and Bogaerts (2014). Charged particle kinetics includes electron-impact ionisation, attachment and dissociation, electron–ion recombination, ion transfers, detachment, ion–ion recombination and associative ionisation. The rate coefficients and electron-impact cross sections considered for those reactions are adopted from Viegas *et al* (2020), Vialetto *et al* (2020). Electron–electron collisions are not considered, as they are not expected to affect rate coefficients in the conditions of interest beyond an increase of 5%. As in Viegas *et al* (2020), molecules are vibrationally populated according to a Boltzmann distribution at T_g for which concerns electron kinetics, in agreement with the temperature measurements in van den Bekerom *et al* (2020), van de Steeg *et al* (2020). Nevertheless, their excited states, as those of C, are not considered for chemical calculations. We thus assume that the radiative emission of O in this plasma is independent of those states and is mostly due to processes affecting exclusively O states. As such, a CRM for atomic oxygen and the excited states listed in table 2 is added in this work, inspired on the recent works of Caplinger and Peram (2020) and of Fiebrandt *et al* (2020). As in Viegas *et al* (2020), no wall reactions are considered, since the contracted

Table 4. List of atomic oxygen quenching reactions. $O(i)$ and $O(j)$ represent any state of atomic oxygen listed in table 2 and M represents any neutral species, except when a note is added. The units of rate coefficients are $\text{cm}^3 \text{s}^{-1}$. T_g is the gas temperature in K.^{a,b}

Nbr	Reaction	Rate coefficient	References
Q1	$O(3p^3P) + M \rightarrow O(3p^5P) + M$	6×10^{-11}	[15, 16]
Q2	$O(3d^3D^0) + M \rightarrow O(3d^5D^0) + M$	6×10^{-11}	[15, 16]
Q3	$O(2p^4^1D) + M^b \rightarrow O(2p^4^3P) + M^b$	$2.60 \times 10^{-11} \times \exp^{67/T_g} + 10^{-12}$	[15, 17]
Q4	$O(2p^4^1D) + O \rightarrow O(2p^4^3P) + O$	8×10^{-12}	[15, 17]
Q5	$O(2p^4^1D) + C \rightarrow O(2p^4^3P) + C$	2.30×10^{-11}	[15, 17]
Q6	$O(2p^4^1S) + M^b \rightarrow O(2p^4^3P) + M^b$	$4 \times 10^{-12} \times \exp(-865/T_g)$	[15, 17]
Q7	$O(2p^4^1S) + O \rightarrow O(2p^4^1D) + O(2p^4^1D)$	$5 \times 10^{-11} \times \exp(-301/T_g)$	[15, 17]
Q8	$O(2p^4^1S) + C \rightarrow O(2p^4^3P) + C$	10^{-12}	[15, 17]
Q9	$O(i)^c + O_2 \rightarrow O(2p^4^3P) + O_2$	2.20×10^{-10}	[15, 18]
Q10	$O(i)^c + CO_2 \rightarrow O(2p^4^3P) + CO_2$	5.30×10^{-10}	[15, 18]
Q11	$O(i)^c + CO \rightarrow O(2p^4^3P) + CO$	8.30×10^{-11}	[15, 18]
Q12	$O(i)^c + O \rightarrow O(2p^4^3P) + O$	2.20×10^{-10}	[15, 18]
Q13	$O(i)^c + C \rightarrow O(2p^4^3P) + C$	3.50×10^{-11}	[15, 18]
Q14	$O(i)^d + M^e \rightarrow O(2p^4^3P) + M^e$	10.80×10^{-10}	[15, 16]
Q15	$O(i)^f + M^e \rightarrow O(2p^4^3P) + M^e$	9.30×10^{-10}	[15, 19]
Q16	$O(i)^g + C \rightarrow O(2p^4^3P) + C$	5.90×10^{-10}	[15, 19]

^aReferences: [15] = Caplinger and Perram (2020); [16] = Dagdigian *et al* (1988); [17] = Gordiets *et al* (1995); [18] = Mori *et al* (1992); [19] = Niemi *et al* (2001).

^bNotes on the species or states considered: b— CO_2 , CO and O_2 ; c— $O(3s^5S^0)$ and $O(3s^3S^0)$; d— $O(3p^5P)$ and $O(3d^3D^0)$; e— CO_2 , CO , O_2 and O ; f— $O(3p^3P)$ and $O(3d^3D^0)$; g— $O(3p^5P)$, $O(3p^3P)$, $O(3d^5D^0)$ and $O(3d^3D^0)$.

MW plasma has no direct interaction with the reactor walls. Together with the reaction scheme in Viegas *et al* (2020), a total of 225 reactions is considered in our model. The reactions of the CRM are listed in tables 3 and 4 and have been defined according to the following considerations:

- The cross sections for excitation and ionisation of ground-state atomic oxygen by electron impact have been retrieved from Laher and Gilmore (1990), where a critical review of experimental and theoretical work on this subject has been presented. Superelastic cross sections are calculated with the formula of Klein–Rosseland (Capitelli *et al* 2015), by considering micro-reversibility. The electron kinetics solver considers separate transitions between the ground-state and all the non-Rydberg states and all the Rydberg states with a $O^+(4S^0)$ core, which is consistent with the set in Alves *et al* (2016) where all these Rydberg states are lumped together. Rydberg states with $O^+(2D^0)$ and $O^+(2P^0)$ cores are taken into account as lumped states, as in Alves *et al* (2016). The double ionisation cross section presented in Laher and Gilmore (1990) is not considered, due to its very high threshold of around 50 eV.
- The CRM considers that $O(3d^5D^0)$ electron-impact excitation includes the excitation to $O(4s^5S^0)$, $O(4p^5P)$ and $O(4d^5D^0)$, as a way to account for radiative cascading of all quintuplet states above $O(3p^5P)$, as in Fiebrandt *et al* (2020). This approach assumes that the upper states relax via radiative processes. The same is done for $O(3d^3D^0)$, including states $O(4s^3S^0)$, $O(4p^3P)$ and $O(4d^3D^0)$. The relevance of cascade emission has been put forward by both Fiebrandt *et al* (2020) and Caplinger and Perram (2020).
- Electron-impact collisions with excited states, shown to be relevant in Caplinger and Perram (2020), are also considered. The elastic cross sections are considered as being the same as for the ground-state, taken from Alves *et al* (2016). The following stepwise excitation collision cross sections have been retrieved from Barklem (2007), as in Caplinger and Perram (2020), Fiebrandt *et al* (2020): $O(2p^4^1D) \rightarrow O(2p^4^1S)$, $O(3s^3S^0)$, $O(3p^3P)$; $O(2p^4^1S) \rightarrow O(3p^3P)$; $O(3s^5S^0) \rightarrow O(3s^3S^0)$, $O(3p^5P)$, $O(3p^3P)$; $O(3s^3S^0) \rightarrow O(3p^5P)$, $O(3p^3P)$; $O(3p^5P) \rightarrow O(3p^3P)$. They have been calculated in Barklem (2007) through a 38-state R-matrix calculation. In the cases where literature sources did not include data tables, cross sections have been digitised from figures. The remaining stepwise excitation and ionisation cross sections are taken as the same as those for electron impact with the ground-state of O from Laher and Gilmore (1990). The same approach to cascade emission is used for stepwise excitation as for ground-state excitation.
- Electron-impact dissociation of CO_2 and CO (reactions O3–O4), using the cross sections in the review of McConkey *et al* (2008), produce the $O(2p^4^1S)$ state.
- The electron-impact cross sections for dissociation of O_2 into $O(2p^4^3P) + O(2p^4^3P)$ and $O(2p^4^3P) + O(2p^4^1D)$ (reaction O5), which are the most populated states of atomic oxygen, are taken from Alves *et al* (2016). Then, for the production of $O(2p^4^1S)$, $O(3p^5P)$ and $O(3p^3P)$ (O5), the dissociative cross sections in McConkey *et al* (2008) are considered. Finally, we take into account electron-impact dissociation of O_2 into the metastables $O(3s^5S^0)$ and $O(3s^3S^0)$ using the emission cross sections from Itikawa (2009), Kanik *et al* (2003). This choice of cross sections is the same as in Fiebrandt *et al* (2020) and

in Stancu *et al* (2016) and is similar to the one in Caplinger and Perram (2020). While in Fiebrandt *et al* (2020) a Maxwellian EEDF is assumed to obtain expressions for rate coefficients, in this model we calculate all electron-impact rate coefficients from the EEDF calculated through the MCF method.

- No kinetic data has been found in literature for production of excited states of O from dissociative electron-ion recombination. The exceptions are the reactions listed in Annušová *et al* (2018) and included in table 3 as O6–O7 for O_2^+ recombination. We should notice that this is the dominant ion in the studied plasma (Viegas *et al* 2020).
- The Einstein coefficients for spontaneous emission are taken from the NIST database (Kramida *et al* 2020). Only transitions with Einstein coefficient above 10^5 s^{-1} have been selected (R1–R6 in table 3). The remaining transitions in the NIST database have Einstein coefficient below 10^4 s^{-1} and thus have been neglected. In fact, the emission intensities of the transitions with wavelengths 777 nm, 845 nm and 926 nm (R1–R3) are measured in the experiments in the CO_2 MW plasma reactor. The measurements are not sensitive to the wavelengths of reactions R4–R6, but the importance of these transitions cannot be excluded.
- The influence of self-absorption on transitions R1–R6 is considered as in Fiebrandt *et al* (2020), where it has been shown to be important. Radiation emitted from a higher level p to a lower level k , of multiplet component l , can be reabsorbed by the lower state to repopulate the higher state. This process limits the number of photons effectively travelling through the plasma. In this work we take it into account by adding a local correction called escape factor $\gamma_{pk,l}(r)$, depending on the number density of the lower level at each position r , such that every coefficient $\tau_{radpk}^{-1}(r)$ in table 3 is defined as:

$$\tau_{radpk}^{-1}(r) = \sum_l A_{pk,l} \gamma_{pk,l}(r) \frac{g_{p,l}}{\sum_l g_{p,l}}, \quad (19)$$

where $A_{pk,l}$ is the Einstein coefficient of each transition from state p to state k , of multiplet component l , found in NIST; $\gamma_{pk,l}$ is the associated escape factor and $g_{p,l}$ is the statistical weight of the upper state in the corresponding transition. To calculate $\gamma_{pk,l}$, we use the same approach as in Fiebrandt *et al* (2020), an approximated empirical formula determined by Mewe (Mewe 1967). In Mewe (1967), the formula assumes homogeneous density profiles of both the upper and the lower state. Then, in Sushkov *et al* (2013), it has been shown that the approximation is valid with any spatial profile of the states densities, as long as the upper and lower states have similar spatial profiles. It has also been estimated that in the worst case scenario, this empirical formula is approximately a factor of 2–3 off to the correct escape factor. In this work, this method is used due to its simplicity, and, as we use this approximation in the 1D model, we take the local densities

at each position r , such that:

$$\gamma_{pk,l}(r) = \frac{2 - \exp(-10^{-3} k_{pk,l}(r) \Lambda_{777})}{1 + k_{pk,l}(r) \Lambda_{777}} \quad (20)$$

$$k_{pk,l}(r) = \frac{\lambda_{pk,l}^2}{8\pi} P_{pk,l}(r) \frac{g_{p,l}}{g_{k,l}} n_{k,l}(r) A_{pk,l} \quad (21)$$

$$n_{k,l}(r) = n_k(r) \frac{g_{k,l}}{\sum_l g_{k,l}} \quad (22)$$

$$P_{pk,l}(r) = \lambda_{pk,l} \sqrt{\frac{m_O}{2\pi k_B T_g(r)}} \quad (23)$$

$k_{pk,l}$, $\lambda_{pk,l}$ and $P_{pk,l}$ are the absorption coefficient, the wavelength and the spectral line profile of the associated transition. $P_{pk,l}$ has been taken as in Fiebrandt *et al* (2017), assuming Doppler broadening as the dominant line broadening mechanism. Λ_{777} is the measured FWHM of the 777 nm emission, here taken as an approximate thickness of the plasma in the radial direction, over which photons are absorbed. m_O is the mass of atomic oxygen, k_B is the Boltzmann constant and $n_{k,l}$ is the number density of species k in the multiplet component l , estimated from the statistical weights $g_{k,l}$.

- Numerical simulations in the conditions studied in this work show that, using the described approach, the effective escape factors can go down to 0.5 in the case of transitions R1–R2 in the centre of the discharge. The escape factors increase radially to approximately 1 on the edges. For transitions R3–R4, with radiative lower state, the escape factor is always close to 1. For the cases of transitions R5–R6, where the lower state is the ground-state, the emission is decreased by about 90% (escape factor of ~ 0.1). The approach used in Santos *et al* (2014) has also been tested, yielding no self-absorption for R1–R4 and complete self-absorption for R5–R6. It has been discarded, since it is only valid for high levels of radiation trapping.
- For the quenching rate coefficients, we use those compiled in Caplinger and Perram (2020). We should notice that many rate coefficients are not reported in literature and many are measured at 300 K only and thus have no temperature dependence. The quenching rate coefficient for excitation transfer Q1 (table 4) is taken from Dagdigan *et al* (1988), where it has been measured with O_2 as collision partner from the ratio of the 777 nm and 845 nm emission intensities. The important role of this reaction has been put forward in Caplinger and Perram (2020). As this rate coefficient hasn't been found in literature for the other collision partners (CO_2 , CO , O and C), we have taken the same rate coefficient for all collision partners. In Morillo-Candas *et al* (2019), the quenching rate coefficient of reaction $O(3p^5P) + M \rightarrow O(2p^4P) + M$, has been measured in low pressure DC glow discharges in O_2 and in CO_2 from the analysis of the temporal decay of fluorescence signals. It has been found to have very similar values in the different mixtures, which reinforces our

assumption of assuming the same rate coefficient for different collision partners. Moreover, we have assumed the same rate coefficient for reactions Q1 and Q2, due to the similarity of the states involved.

- For the quenching reactions of $O(2p^4\ ^1D)$ and $O(2p^4\ ^1S)$ (Q3–Q8), the rate coefficients used in the model of Gordiets *et al* (1995) are taken. The coefficients for collision partners CO and CO₂ are considered as being the same as for O₂, according to the same reasoning followed for Q1. When C is the collision partner, the rate coefficients for N or N₂ quenchers is taken. We should notice that C has a low molar fraction in the current study, when compared to the other neutrals.
- The quenching rate coefficients of the higher metastable $O(3s\ ^5S^0)$ (Q9–Q13) are taken from Mori *et al* (1992), where they have been measured for O₂, CO, CO₂ and N₂ quenchers from absorption decay curves. For O and C quenchers, the coefficients from O₂ and N₂ are considered, respectively. Furthermore, we assume the rate coefficients for the remaining metastable ($3s\ ^3S^0$) to be equal to those for $O(3s\ ^5S^0)$, as in Caplinger and Perram (2020).
- Finally, for the quenching of the radiative states (Q14–Q16), the quenching coefficients with O₂ are considered, measured for $O(3p\ ^5P)$ in Dagdigian *et al* (1988) and for $O(3p\ ^3P)$ in Niemi *et al* (2001). As for the other quenching reactions, we assume the same rate coefficient for O₂ quencher and for CO₂, CO and O quenchers. For C quencher, the coefficient with N₂ quencher measured in Niemi *et al* (2001) is taken for all radiative states.
- A simple sensitivity analysis study has been performed on the quenching rate coefficients. Simulations have been run while replacing a few quenching coefficients by the corresponding ones from different sets (Dagdigian *et al* 1988, Pietanza *et al* 2020, Fiebrandt *et al* 2020). It has been verified that this leads to no relevant difference in the simulation results in this work, which suggests that an eventual temperature dependence of these coefficients would not affect the conclusions obtained in this work.

4. Results

In this section, we apply the model previously described to the different plasma conditions A, B and C explained in section 2.2. Firstly, the initial assumptions of $n_e(r)$ are used. The relationship between $n_e(r)$ and $I_{777}(r)$ is obtained from simulation results and used to correct the input profile of $n_e(r)$ consistently with the measured Gaussian profile of $I_{777}(r)$. This process is explained in detail for the low-confinement discharge of condition A, for which several spatially-resolved discharge parameters are provided from the simulation results. Then, the same procedure is applied to the high-confinement discharge of condition B and to the wider parameter range of set C. In the case of set C, it is shown that the findings from this study have a direct impact on the flow simulations that provide input T_g

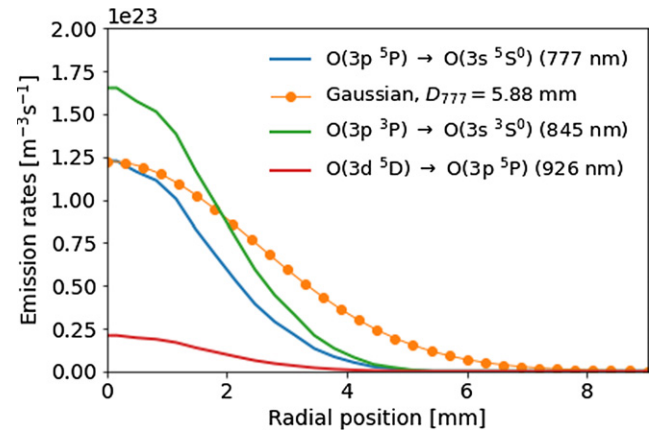


Figure 4. Radial profiles of the simulated emission rates corresponding to the radiative transitions of wavelength 777, 845 and 926 nm, for condition A (950 W, 9 slm and 100 mbar). A Gaussian curve with the measured Λ_{777} is also presented.

and composition, and hence the flow model and the procedure to correct spatial profiles of discharge parameters are interdependent. Overall, this study allows both to quantify the impact of parameter changes in the relationships between discharge parameters, and to generalise certain conclusions about the spatial resolution of those parameters and its potential impacts on the study of plasmas for CO₂ conversion.

4.1. Condition A: low-confinement discharge

4.1.1. Using initial assumptions. We start by using the plasma model to study the low-confinement discharge of condition A, described in section 2.2. The assumption that $n_e(r)$ follows the same Gaussian profile as the measured $I_{777}(r)$ (equation (8)) is taken as a starting point for the model input. Figure 4 depicts the emission rates of the three transitions identified in experiments (R1–R3 in table 3), obtained as simulation results, which have the same FWHM as the corresponding emission intensities. A Gaussian profile with the same peak as the simulated 777 nm emission rate and with the measured FWHM, $\Lambda_{777} = 5.88$ mm, is added, for comparison with the simulation results.

The results in figure 4 show that the numerically-obtained emission rates have seemingly Gaussian radial profiles, as in the experiments. Moreover, the ratios between the three emission rates agree qualitatively with experimental measurements. However, it is visible that the simulated emission rate of the 777 nm transition has a narrower radial profile than the measured emission intensity. This result suggests that the initial assumption on input $n_e(r)$ (linearly proportional to $I_{777}(r)$) is incorrect. Indeed, the input taken from equation (8) assumes that n_e and I_{777} are linearly proportional. In figure 5, the dependence of the three considered emission rates on n_e is presented. The simulation results have been fitted in order to derive the proportionality parameter s from equation (5), and we found the best fits to result from polynomial functions of second order. The fits are included in figure 5. According to these fits, the emission rates of the 777, 845 and 926 nm transitions,

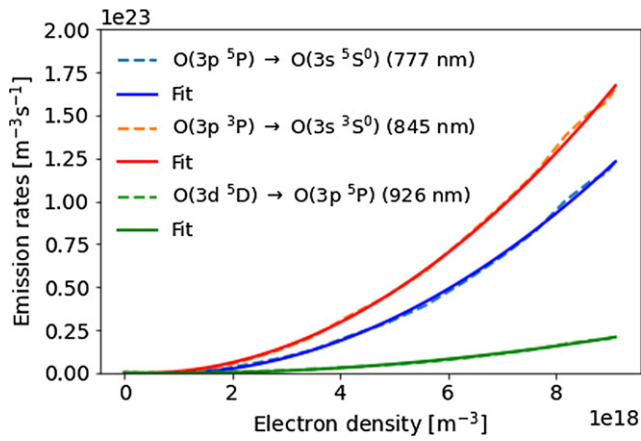


Figure 5. Emission rates corresponding to the radiative transitions of wavelength 777, 845 and 926 nm, as function of n_e , for condition A (950 W, 9 slm and 110 mbar). Simulation results and polynomial fits.

respectively, R_{777} , R_{845} and R_{926} , are given in $\text{m}^{-3} \text{s}^{-1}$ by:

$$R_{777}(n_e) = -2259 (\text{s}^{-1}) \times n_e (\text{m}^{-3}) + 1.731 \times 10^{-15} (\text{m}^3 \text{s}^{-1}) \times n_e^2 (\text{m}^{-6}) \quad (24)$$

$$R_{845}(n_e) = -1308 (\text{s}^{-1}) \times n_e (\text{m}^{-3}) + 2.161 \times 10^{-15} (\text{m}^3 \text{s}^{-1}) \times n_e^2 (\text{m}^{-6}) \quad (25)$$

$$R_{926}(n_e) = -516.5 (\text{s}^{-1}) \times n_e (\text{m}^{-3}) + 3.076 \times 10^{-16} (\text{m}^3 \text{s}^{-1}) \times n_e^2 (\text{m}^{-6}). \quad (26)$$

Figure 5 shows that the polynomial functions provide good fits to the simulation results. Furthermore, it is demonstrated that the dependence of the emission rates on n_e is not linear, but rather closer to quadratic, and thus the assumption taken on the profile of $n_e(r)$ should be corrected. This dependence will be explained in the next paragraphs, after correcting the input profile of $n_e(r)$.

4.1.2. Corrections to assumptions. The assumption on $n_e(r)$ that is taken as input in the model can be corrected based on the fits shown previously. Indeed, as we have described $R_{777}(n_e)$ as a polynomial of second order, n_e can also be described as a polynomial of second order of $R_{777}^{1/2}$, with fitting parameters c_1 and c_2 , of the form:

$$n_e = c_1 \times R_{777}^{1/2} + c_2 \times R_{777}. \quad (27)$$

By assuming $R_{777}(r)$ to follow a Gaussian profile of FWHM Λ_{777} and characteristic width σ_{777} (equation (1)), and then line-integrating equation (27) considering the measured $n_{e\Lambda}$, we obtain:

$$n_{e\Lambda} = c_1 \times R_{777}^{1/2}(0) \sqrt{4\pi\sigma_{777}} + c_2 \times R_{777}(0) \sqrt{2\pi\sigma_{777}}. \quad (28)$$

$R_{777}(0)$ can be directly obtained from this equation. Then, equation (27) yields a new profile for $n_e(r)$, that consists of a superposition of two Gaussian curves of different FWHM and

that stems directly from the simulation results using the previous assumption for $n_e(r)$. We should notice that n_{e0} of the new profile is different than the one firstly assumed, but the measured line-integral $n_{e\Lambda}$ is conserved. In the case of condition A using the initial assumption for $n_e(r)$, the simulation results yield $c_1 = 3.097 \times 10^7 \text{ m}^{-3/2} \text{ s}^{1/2}$ and $c_2 = -1.861 \times 10^{-5} \text{ s}$. Using these values, a new profile of $n_e(r)$ is used as input for the simulations. Then, as the second iteration of simulation results does not yet provide an agreement of the $R_{777}(r)$ profile with experiments within 5%, this procedure is repeated until that condition is satisfied. For the case of condition A, 3 simulations were required to find a satisfying $R_{777}(r)$ profile. The succeeding $n_e(r)$ and $R_{777}(r)$ profiles are presented in figure 6.

As we can notice from figure 6, the applied correction procedure results in a broadening of the input $n_e(r)$ and of the output $R_{777}(r)$, until the emission rate approximately matches a Gaussian curve with FWHM of Λ_{777} , the one measured for emission intensity. This procedure is proven to successfully reproduce the measured radial profile of R_{777} . As such, this model can radially resolve discharge parameters. In fact, the $n_e(r)$ profile that matches the measured output can be approximately described as a Gaussian profile with FWHM = 9.93 mm, i.e. with an FWHM value 1.69 times higher than the one of R_{777} . Consequently, as $n_{e\Lambda}$ is conserved in equation (6), the peak n_{e0} is lower than initially assumed, by approximately the same factor of 1.69. Following equation (2), the proportionality parameter s is calculated as $1.69^2 \simeq 2.85$, close to the stated upper limit of 2. The fact that $n_e(r)$ follows a seemingly Gaussian profile agrees with previous studies of contracted discharges at intermediate to high pressures in Petrov and Ferreira (1999), Martinez *et al* (2004), Kabouzi *et al* (2007), Dyatko *et al* (2008), Golubovskii *et al* (2011), Shneider *et al* (2014), Golubovskii *et al* (2017), Ridenti *et al* (2018), Zhong *et al* (2019). Furthermore, we find n_e to have a broader radial profile than the emission intensity, which consists in the phenomenon of optical contraction reported in Golubovskii *et al* (2011, 2020). It is also visible in figure 6 that, besides the Gaussian fit, $n_e(r)$ can also be fitted by a Bessel function or by a paraboloidal function (not shown), in agreement with the radially-resolved n_e Thomson scattering measurements in the argon MW discharge in Carbone *et al* (2012). However, unlike the Gaussian fit, these functions become negative well before reaching the walls, which is not compatible with the presence of diffusive transport. As such, we deem it more fit to describe the radial profiles of n_e as Gaussian functions.

4.1.3. Kinetics of O emission intensity. To understand the proportionality parameter s around 2.85, the main reaction rates of production and destruction of the upper state of the 777 nm transition, O(3p ^5P), are presented in figure 7, from the simulation results of iteration 3.

Figure 7 shows that the main production reactions of O(3p ^5P) are electron-impact reactions, firstly through electron impact with the ground-state of atomic oxygen, and then through collisions with the higher metastables O(3s $^5\text{S}^0$) and O(3s $^3\text{S}^0$). This result highlights the relevance of stepwise excitation put forward in Caplinger and Perram (2020) and shown for O(3p ^3P) in Fiebrandt *et al* (2020). Quenching from upper

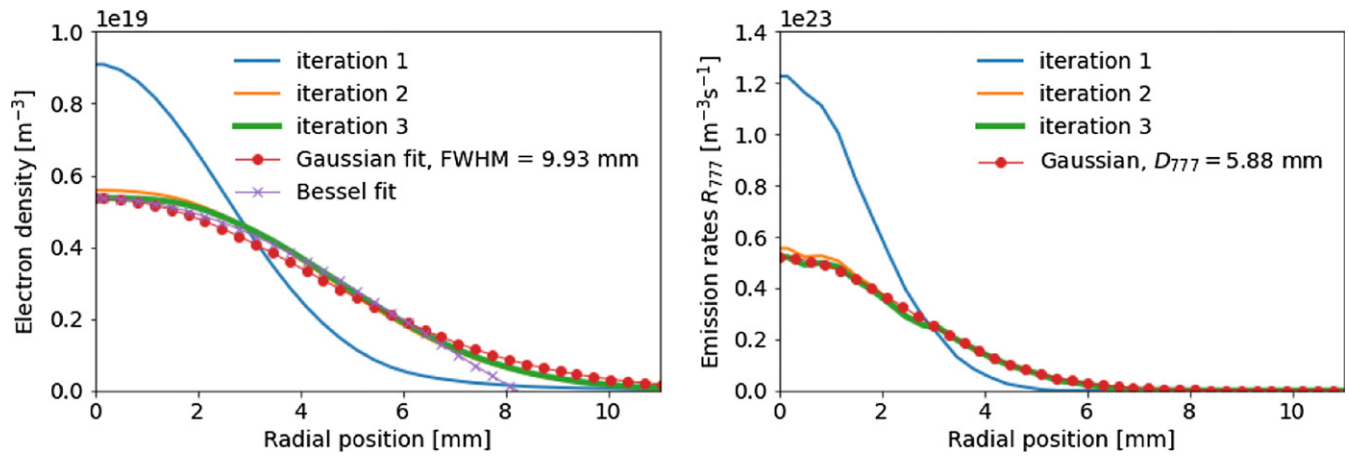


Figure 6. Radial profiles of n_e (on the left) and R_{777} (on the right) for successive iterations, for condition A (950 W, 9 slm and 110 mbar). Each iteration corresponds to a different input $n_e(r)$. A Gaussian function and a Bessel function have been fitted to the last profile of $n_e(r)$. A Gaussian curve with experimentally-obtained Λ_{777} is also compared to the last result of $R_{777}(r)$.

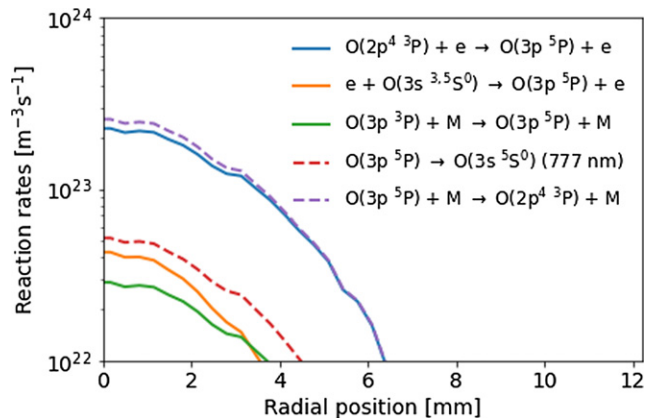


Figure 7. Radial profiles of the main rates of source and loss of the upper radiative state of the 777 nm transition, $O(3p^5P)$, for condition A (950 W, 9 slm and 110 mbar). Production rates in solid lines and loss rates in dashed lines. Simulation results from iteration 3.

states (reaction Q1 in table 4) and emission from upper states (R3, not shown in figure 7) also populate $O(3p^5P)$, although this last reaction contributes to less than 5% of production. Therefore, cascade emission populating the upper states also influences the production of $O(3p^5P)$, as highlighted in both Fiebrandt *et al* (2020) and Caplinger and Perram (2020). Other production mechanisms of $O(3p^5P)$ that have been considered in the simulations, such as dissociative excitation and other electron-impact reactions, appear to play a negligible role. As far as losses are concerned, the main mechanisms are quenching and radiative emission. Radiation self-absorption has a role in these simulations, confirming the importance attributed to it in Fiebrandt *et al* (2020). Indeed, the emission coefficient τ_{rad}^{-1} of the 777 nm transition in condition A is a function of r . τ_{rad}^{-1} is $3.38 \times 10^7 \text{ s}^{-1}$ at $r = 0$ and increases to its natural value of $3.69 \times 10^7 \text{ s}^{-1}$ for $r > 5$ mm. Other loss processes of $O(3p^5P)$ included in the model, through transport (convective and diffusive) and electron impact, are shown to have a lesser role for $O(3p^5P)$ balance. Overall, we can say that

hypothesis 1 in section 2.1 on the 777 nm radiation balance is approximately verified, as it correctly estimates the importance of direct electron-impact excitation, quenching and emission from $O(3p^5P)$, but neglects the secondary role of stepwise excitation and of the states above $O(3p^5P)$.

Hypothesis 2 is also approximately verified, although τ_{rad}^{-1} is not radially homogeneous. Indeed, quenching is the main loss process ($n_g k_Q > \tau_{\text{rad}}^{-1}$) and k_Q is approximately radially homogeneous. Thus, if we consider an effective electron-impact excitation coefficient $k_{\text{eff}}(T_e)$ including stepwise excitation, we can write:

$$I_{777} \propto \tau_{\text{rad}}^{-1} n_e x_O k_{\text{eff}}(T_e). \quad (29)$$

In the plasma, as we approach the centre, n_e increases and τ_{rad}^{-1} slightly decreases. Then, in figure 8, we evaluate the radial dependence of T_e (2/3 of the electron mean energy), of E/n_g and of the electric field magnitude E , as well as the dependence of the electron-impact excitation coefficient on n_e . The impact of stepwise excitation is highlighted by depicting both the ground-state electron-impact excitation coefficient to $O(3p^5P)$, k_{exc} , and the effective coefficient including also excitation from the higher metastables, k_{eff} .

The simulation results in figure 8 indicate that T_e and E/n_g in the CO_2 MW discharge have concave shapes as in the studies of contracted discharges in Kabouzi *et al* (2007), Gregório *et al* (2010), Golubovskii *et al* (2011), Gregório *et al* (2012), Golubovskii *et al* (2017), Ridenti *et al* (2018), Zhong *et al* (2019), Golubovskii *et al* (2020), due to the self-reinforcing cycle between heating and electron-driven collisionality. However, here the electric field magnitude presents a rather flat profile in the whole plasma region up to $r = 10$ mm. We should notice that for higher radial positions, where $n_e(r) \leq 7 \times 10^{16} \text{ m}^{-3}$ and no electron-impact ionisation takes place, the simulation result of E/n_g is assumed to have a minimum value of 1 Td, which also affects the calculation of T_e and E . Conversely, in the 3D EM simulation results in Groen *et al* (2019), addressing a low-confinement discharge in the same MW reactor and assuming equation (8) as input profile, E/n_g and E have rather flat profiles only in the first 4 mm near the axis, and then a

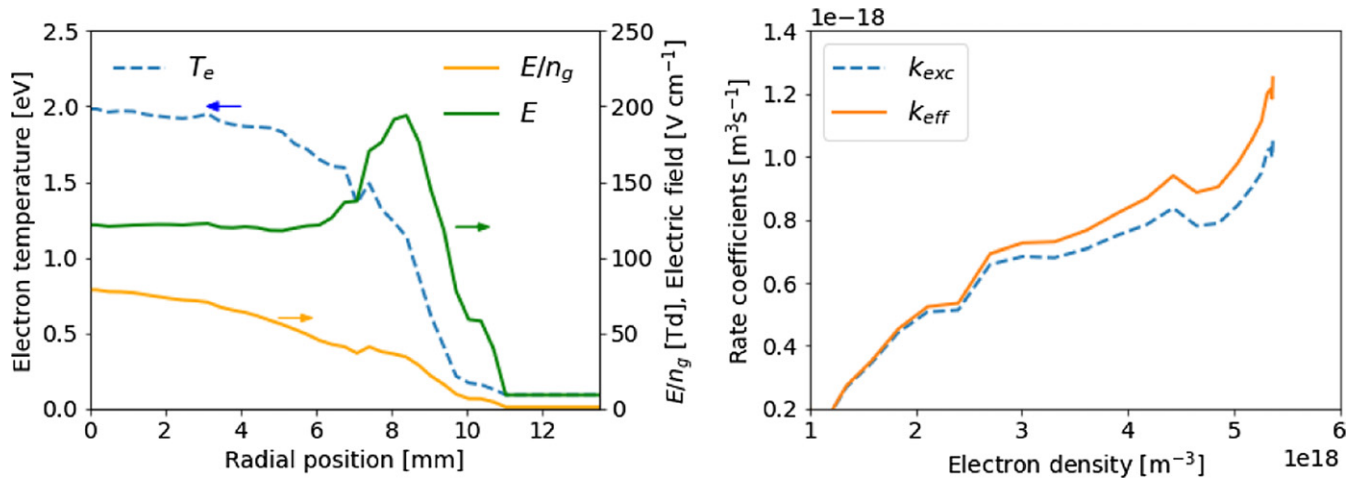


Figure 8. On the left, radial profiles of T_e , E/n_g and E . On the right, electron-impact excitation coefficients of $O(3p^5P)$, as function of n_e . k_{exc} is the coefficient corresponding to excitation from ground-state only. k_{eff} is an effective coefficient, corresponding to excitation from ground-state $O(2p^4\ ^3P)$, $O(3s\ ^5S^0)$ and $O(3s\ ^3S^0)$. Simulation results from iteration 3.

convex shape radially outwards. Moreover, the values of E/n_g and E reported in that work are close to twice as much as those shown here. These discrepancies and the importance of the current study for the results in Groen *et al* (2019) are discussed in section 4.4.

Figure 8 also shows that, as E/n_g increases towards the axis where n_e is also higher, the electron-impact excitation coefficients increase almost linearly with n_e . The increase of k_{exc} and k_{eff} is expected in the context of contracted discharges where gas heating and electron-driven collisionality reinforce each other and where the electron-impact ionisation coefficient also needs to increase to maintain a higher n_e (Viegas *et al* 2020). This relationship means that the main production channels of $O(3p^5P)$ cannot be considered radially homogeneous, which invalidates hypothesis 3 in section 2.1. It also shows that the concave shape of both E/n_g and n_e is the main reason for the optical contraction phenomenon observed in this work, which is in agreement with the analysis reported in Golubovskii *et al* (2020) concerning helium glow discharges.

The last element to analyse in equation (29) is the molar fraction of atomic oxygen x_O , that has been measured and shown to have a concave profile in figure 2. If we consider a plasma region of 5.1 mm radius where n_e is halved (figure 6), x_O drops radially in the same region also by approximately a factor 2 (figure 2). Indeed, n_e and x_O have rather similar radial profiles. As assumed in hypothesis 4, x_O is defined by thermal chemistry and charged particle kinetics, in addition to a contribution of transport which remains largely unknown in this reactor. Hence, the large radial variations of T_g justify the approximately linear correlation between n_e and x_O . This assessment allows to explain, from equation (29), why the proportionality parameter s between I_{777} and n_e is found to be close to 2.85. As the radial position approaches the centre and n_e increases, although τ_{rad}^{-1} slightly decreases, x_O and k_{eff} increase proportionally to n_e , justifying a proportionality parameter between 2 and 3. We should notice that this conclusion holds despite the experimental uncertainty in input parameters, as the proportionality between emission intensity and n_e

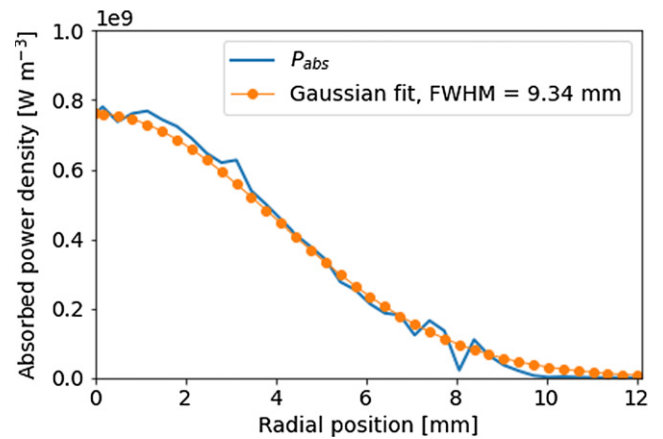


Figure 9. Radial profile of absorbed power density for condition A (950 W, 9 slm and 110 mbar) and Gaussian fit. Simulation results from iteration 3.

is mostly dependent on the shape of radial profiles, which is independent of the absolute value of $n_{e\Delta}$ and of the relatively low experimental uncertainties in T_g and composition.

4.1.4. Power density profile. Another very important parameter for MW discharge characterisation that is affected by the optical contraction, due to its proximity to n_e , is the absorbed power density, P_{abs} . In figure 9 we assess the radial profile of $P_{abs}(r)$, calculated according to equation (18).

Figure 9 shows that $P_{abs}(r)$ can also be approximated as a Gaussian curve for condition A, with an FWHM $\Delta_{P_{abs}} = 9.34$ mm, very close to the one of n_e . Indeed, we find an FWHM 1.59 times higher than Δ_{777} and thus a proportionality $I_{777} \propto P_{abs}^{sp}$, $s_p \simeq 2.5$. Following equation (18), and considering that the electron transport terms have a weight of only 2% on the calculation of P_{abs} , we can write $P_{abs}(r) \simeq \left(\frac{P_{el}}{n_g}(r) + \frac{P_{inel}}{n_g}(r) + \frac{P_{growth}}{n_g}(r) \right) n_g(r)n_e(r)$. We should notice that the collisional electron losses increase with E/n_g and thus also with n_e , but n_g is inversely correlated with n_e .

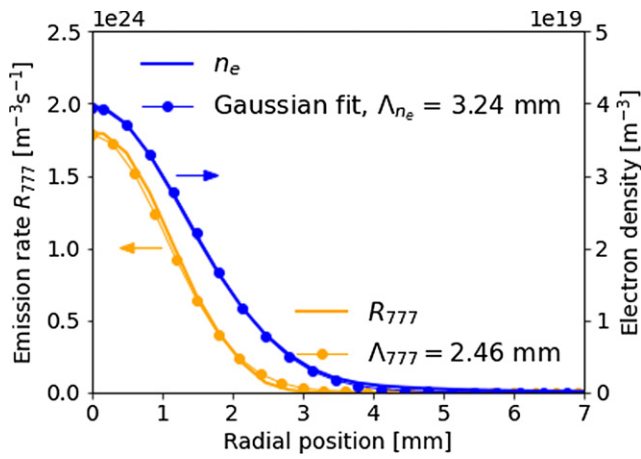


Figure 10. Radial profiles of the 777 nm transition emission rate (left-side axis) and the corrected electron density (right-side axis) for condition B (860 W, 12 slm and 150 mbar). The simulation results after correction procedure and the Gaussian curves with measured FWHM Λ_{777} and fitted FWHM Λ_{n_e} are presented.

These relationships justify a similar but lower proportionality parameter between I_{777} and P_{abs} than between I_{777} and n_e for condition A. The results in this section show that it is relevant to correct the assumptions on the proportionality between I_{777} , n_e and P_{abs} . Moreover, it is demonstrated that we can successfully resolve discharge parameters from I_{777} and the proposed procedure, for the case of a low-confinement discharge.

4.2. Condition B: high-confinement discharge

The confinement degree of the CO₂ MW discharge depends strongly on input power and pressure (Wolf *et al* 2020b). In this section, we evaluate whether the conclusions taken from the study of condition A can be extended to conditions of high-confinement discharges. Starting from the input profile of $n_e(r)$ described in section 2.2, the same correction procedure used for condition A is applied to condition B. After one correction, the $R_{777}(r)$ and $n_e(r)$ profiles represented in figure 10 are obtained. Two Gaussian curves are added to the figure: one with the simulated peak of R_{777} and the measured FWHM Λ_{777} , and one as a fit to the $n_e(r)$ profile.

Similarly to condition A, figure 10 shows that an approximately Gaussian R_{777} radial profile is obtained with the experimental Λ_{777} as FWHM, in the high-confinement condition B. Indeed, the correction procedure we developed is successful in reproducing the experimental profiles for different conditions of power, pressure and confinement degree. The radial profile of n_e is obtained as a Gaussian curve of FWHM $\Lambda_{n_e} > \Lambda_{777}$, which confirms the phenomenon of optical contraction. The ratio $\Lambda_{n_e}/\Lambda_{777}$ for condition B is 1.32 and the proportionality parameter s between n_e and I_{777} ($I_{777} \propto n_e^s$) is 1.74, lower than the corresponding values for condition A (1.69 and 2.85, respectively). The relationship between n_e and I_{777} is also described by equation (29) in condition B, as the main reaction mechanisms for the balance of O(3p⁵P) are the same as for condition A. However, we should notice that stepwise excitation to O(3p⁵P) has a more important role in

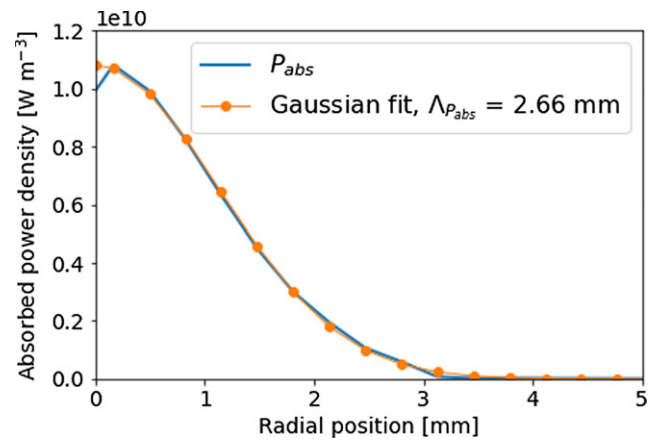


Figure 11. Radial profile of simulated absorbed power density for condition B (860 W, 12 slm and 150 mbar) and Gaussian fit.

high-confinement conditions. Following equation (29), the difference in s between conditions A and B is justified by the different behaviour of τ_{rad}^{-1} and of x_O between these discharges. In fact, the electron-impact excitation coefficient to O(3p⁵P) is approximately linearly proportional to n_e in both conditions A and B. T_e and E/n_g are concave and E is approximately flat within the plasma in both contracted modes. In the case of condition B, T_e and E/n_g have maxima of 2.4 eV and 110 Td, and $E \simeq 140$ V cm⁻¹ for $r < 3$ mm, higher values than for condition A. Contrarily to the low-confinement discharge, these values should not be compared to those found for a high-confinement discharge in Groen *et al* (2019) since significantly higher pressure and lower temperature are considered in that work. The lower proportionality parameter s in the high-confinement condition is justified mostly by the more homogeneous x_O profile revealed in the measurements presented in figure 3. x_O is close to 0.4 for $r < 3$ mm and decreases to 0.2 at $r = 5$ mm, while n_e decreases by two orders of magnitude along the same distance. Moreover, the emission coefficient τ_{rad}^{-1} evolves inversely to n_e , as it falls linearly from its original value of 3.69×10^7 s⁻¹ for $r > 4$ mm to 2×10^7 s⁻¹ at $r = 0$, due to the higher self-absorption in high-confinement conditions. Finally, the simulated power density is also fitted to a Gaussian curve, as shown in figure 11.

Figure 11 shows that the Gaussian curve describing $P_{abs}(r)$ for condition B has $\Lambda_{P_{abs}} = 2.66$ mm, very close to Λ_{777} . Indeed, we find $\Lambda_{P_{abs}}/\Lambda_{777} = 1.08$ and thus $s_p = 1.16$, very close to the initial assumption of $s_p = 1$ (hypothesis 6 in section 2.1). Furthermore, figure 9 shows a dip in the simulated $P_{abs}(r)$ in the axis of the discharge. As noted in the study of condition A, following the electron energy equation (equation (18)), collisional electron losses increase with E/n_g and thus also with n_e , but n_g is inversely correlated with n_e . The sharp gradients of T_g and n_g in high-confinement conditions help explain both the dip in P_{abs} and $\Lambda_{P_{abs}} \ll \Lambda_{n_e}$.

The conclusions from the study of condition A on the most relevant factors to take into account to relate I_{777} and n_e are kept when changing power, pressure and confinement degree in condition B. However, it is shown here that the proportionality between I_{777} , n_e and P_{abs} is not the same in every plasma,

as n_e , T_g and x_O have significantly different profiles according to the confinement degree. Hence, different plasma conditions require dedicated analysis in order to spatially resolve discharge parameters.

4.3. Set of conditions C: interdependence with flow modelling

In the set of conditions C, described in section 2.2, the input of T_g and composition used to resolve discharge parameters is obtained from flow simulations of the model described in Wolf *et al* (2020a). The observed confinement degree in these conditions generally stands between the one of the low-confinement discharge of condition A and that of the high-confinement discharge of condition B. The values and extension of T_g and dissociation degree are also in between those of the two previously studied conditions. As such, by applying the same correction procedure as in the previous sections, we expect to obtain, for the set of conditions C, spatial profiles and proportionality parameters s and s_p in between those found for conditions A and B. Indeed, the Gaussian radial profiles of R_{777} with experimentally-measured Λ_{777} have been obtained for this set of conditions with 3 or 4 iterations of the assumed $n_e(r)$ profiles. As a result, corrected profiles of $n_e(r)$ and $P_{\text{abs}}(r)$ have been retrieved. While $n_e(r)$ is well described by a single Gaussian curve, $P_{\text{abs}}(r)$ for the set of conditions C slightly deviates from this shape, due to the dip at the axis that has been discussed for condition B, and whose depth increases with pressure. Still, the profiles $P_{\text{abs}}(r)$ have been fitted to Gaussian functions with FWHM $\Lambda_{P_{\text{abs}}}$. In figure 12, Λ_{777} , Λ_{n_e} and $\Lambda_{P_{\text{abs}}}$ are compared as function of pressure, and the ratios between these quantities are represented for the set of conditions C.

Figure 12 shows that Λ_{n_e} and $\Lambda_{P_{\text{abs}}}$ are, as Λ_{777} , approximately independent of pressure for pressures above 150 mbar, confirming the conclusion from Wolf *et al* (2019) that Λ_{n_e} is independent of pressure in H-mode conditions. Both Λ_{n_e} and $\Lambda_{P_{\text{abs}}}$ are higher than Λ_{777} , as the discharge is in every case broader than initially assumed. For the set of conditions C, $\Lambda_{n_e}/\Lambda_{777}$ varies between 1.45 and 1.73 and $\Lambda_{P_{\text{abs}}}/\Lambda_{777}$ stands between 1.42 and 1.58. We should notice that the correction procedure leads to a decrease of n_{e0} relative to the initial assumption in the same proportion as the increase in Λ_{n_e} . $P_{\text{abs}0}$ also decreases with the correction procedure, but in a different proportion with respect to $\Lambda_{P_{\text{abs}}}$, since it is a simulation result and no line-integrated conservation is imposed as in the case of n_e . In fact, $P_{\text{abs}0}$ decreases by a factor between 1.6 (for 296 mbar) and 4.7 (for 108 mbar). The values of the ratios $\Lambda_{n_e}/\Lambda_{777}$ and $\Lambda_{P_{\text{abs}}}/\Lambda_{777}$ are very close to those found in the case of the low-confinement discharge in condition A as, following equation (29), x_O and k_{eff} are approximately linearly proportional to n_e , and τ_{rad}^{-1} is convex in the plasma region. We should notice that the $x_O(r)$ profile is a direct input from 2D flow simulations in the set of conditions C. In turn, the flow model takes the $n_e(r)$ and $P_{\text{abs}}(r)$ profiles as input. This has been done firstly using the assumptions from equations (8) and (9), i.e. $\Lambda_{P_{\text{abs}}} = \Lambda_{n_e} = \Lambda_{777}$. In this work, the $n_e(r)$ and $P_{\text{abs}}(r)$ profiles are corrected for the 7 cases of the set of conditions C, using the ratios found here. Indeed, these profiles are taken with approximately 1.6 times higher radial and axial

FWHM, and used as input in the model described in Wolf *et al* (2020a). As n_e is conserved line-integrated and P_{abs} is conserved volume integrated, their peaks are, respectively, around 1.6 and 4 times lower. Different simulation results are obtained with these inputs, with respect to the initial ones using the assumptions from equation (8) and (9). To show the resulting difference, the initial and corrected radial profiles of T_g and x_O at the axial position of highest T_g are represented in figure 13 for 121 mbar and 296 mbar. Besides the importance of x_O and T_g for the study of spatial profiles of discharge parameters, we have seen in figures 2 and 3 that T_g and x_O are correlated with the production of CO, the dissociation product that these reactors are aimed at producing.

In the flow model in Wolf *et al* (2020a), the peak gas temperature is set to the one measured in Doppler broadening measurements (Wolf *et al* 2019). As such, the broader profile of P_{abs} leads to the same peak temperature but a slightly broader high-temperature profile, as shown in figure 13. Although apparently small, this broadening increases thermally-driven dissociation in the plasma and hence produces higher and more extended profiles of O and CO molar fractions, as shown on the right side of the same figure. This effect is reinforced by the broadening of the $n_e(r)$ profile driving electron-impact dissociation reactions.

The changes in temperature and composition have an influence on the study of spatial profiles undergone in the current work, and the two models (flow and plasma) are therefore interdependent. The plasma simulations are run for the corrected cases of the set of conditions C to verify the consistency of our results. For $p < 150$ mbar, the dependence between I_{777} , n_e and P_{abs} is very similar with or without this correction, as the corrected x_O has higher values but a similar radial profile as in the initial assumption. However, for highly-contracted conditions with $p > 150$ mbar, the correction leads to a more flat profile of $x_O(r)$, similar to the one presented in figure 3, and therefore to a dependence between the studied parameters that is closer to that of condition B. As such, in those cases the interdependence between the inputs of the two models is not fully consistent. We can only conclude that the values of the ratios $\Lambda_{n_e}/\Lambda_{777}$ and $\Lambda_{P_{\text{abs}}}/\Lambda_{777}$ stand between those of condition B, respectively 1.32 and 1.08, and those of figure 12, both close to 1.6. Although allowing for the study of a wider parameter range, the interdependence between the two models presents some limitations with respect to using the plasma model with experimentally measured input. Those limitations can be overcome through the development of a self-consistent model simulating flow, temperature, composition and plasma parameters.

Gathering the results of conditions A, B and C, we can say that the proportionality between n_e , P_{abs} and I_{777} can be described as $I_{777} \propto n_e^s$, $1.82 \leq s \leq 2.94$ and $I_{777} \propto P_{\text{abs}}^{s_p}$, $1.22 \leq s_p \leq 2.50$. The disparity between these proportionality parameters shows that the spatial resolution of discharge parameters from emission intensity is rather complex and dependent on particular conditions. As such, spatially-resolved measurements and simulations are two essential and complementary tools to accurately describe the spatial profiles of discharge parameters in contracted plasmas. Moreover, we

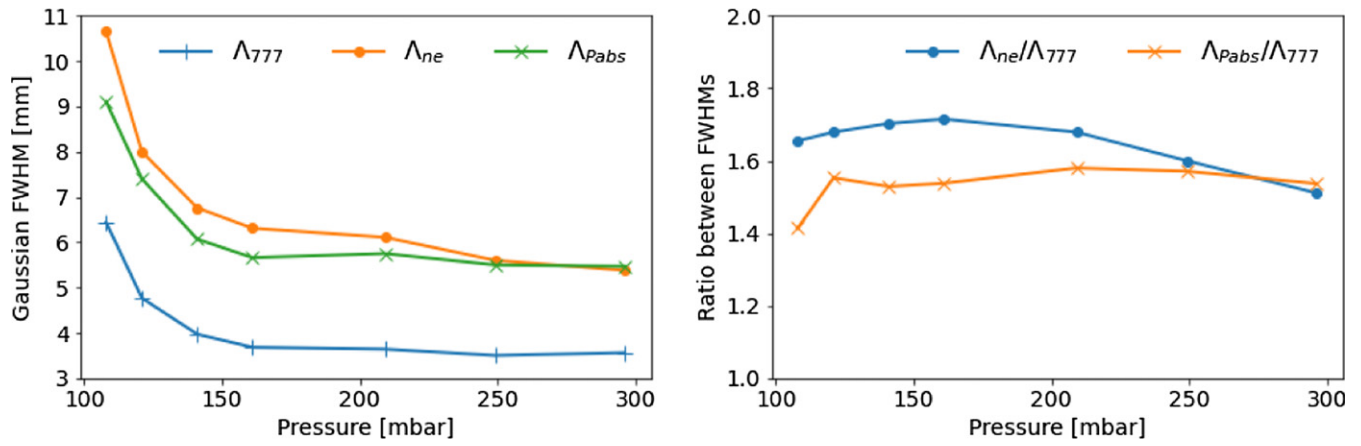


Figure 12. On the left, different diameters as function of pressure, after applying the correction procedure. On the right, the ratios between Λ_{ne} and Λ_{777} and between $\Lambda_{P_{abs}}$ and Λ_{777} , as function of pressure. Results obtained for the set of conditions C.

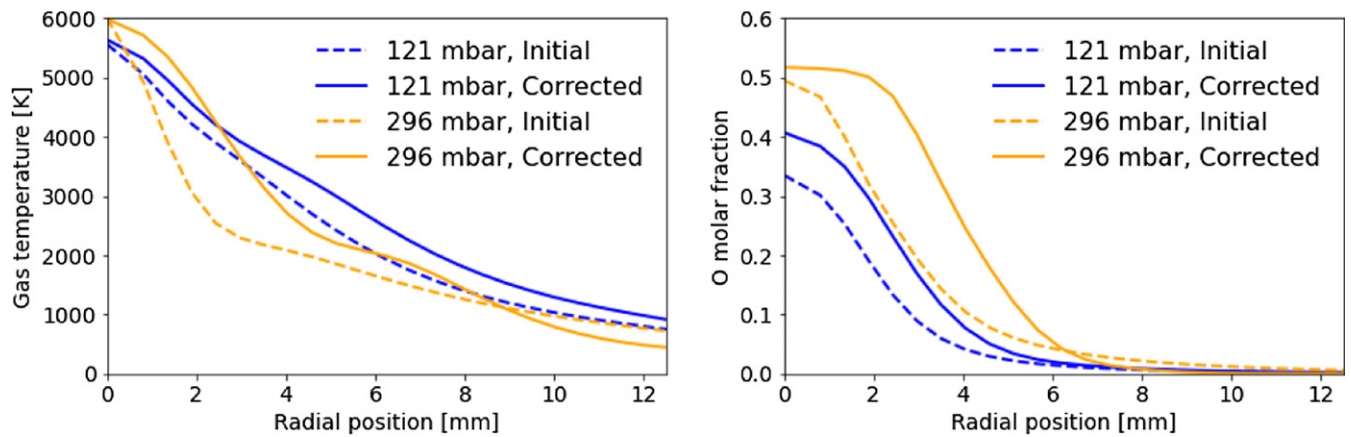


Figure 13. Radial profiles of flow model results, using the initial assumptions on $n_e(r)$ and $P_{abs}(r)$ ($\Lambda_{P_{abs}} = \Lambda_{ne} = \Lambda_{777}$), and the corrected $n_e(r)$ and $P_{abs}(r)$ profiles with $\Lambda_{P_{abs}} \sim \Lambda_{ne} \sim 1.6 \times \Lambda_{777}$. Gas temperature is represented on the left and O molar fraction on the right.

should notice that, despite the complexity, Λ_{ne} and $\Lambda_{P_{abs}}$ are around 1.6 times higher than Λ_{777} for $p < 150$ mbar and the values of the proportionality parameters s and s_p are close to 2.5. Hence, these values can be assumed for MW CO₂ contracted plasmas that are not fully contracted, i.e. whose contraction regime is not H-mode according to the characterisation in Wolf *et al* (2020b). Based on this modelling study, our evaluation of the hypotheses listed in section 2.1 is summarised in table 5.

4.4. Discussion on implications of the correction of radial profiles of plasma parameters

The contracted MW discharges for CO₂ conversion have been studied in detail in the experimental works in Wolf *et al* (2019) and Wolf *et al* (2020b). In Wolf *et al* (2019), the electron density in the MW CO₂ conversion discharge has been measured line-integrated, and its peak n_{e0} has been taken from $n_{e\Lambda}$ (equation (6)) assuming $s = 1$, i.e. that $\Lambda_{ne} = \Lambda_{777}$. This measurement, along with that of T_g in the plasma core through Doppler broadening, has revealed an ionisation degree in the core (n_{e0}/n_{g0}) of the order of 10^{-5} in L-mode conditions

and rising to 10^{-4} in H-mode. Moreover, it has been established in Wolf *et al* (2019) that the plasma radius $\Lambda_{ne}/2$ is of the same order of the skin-depth of MW absorption and that n_{e0}/n_{g0} is approximately inversely proportional to the square of the plasma diameter: $n_{e0}/n_{g0} \propto \Lambda_{ne}^{-2}$. These assertions characterise discharge contracted modes and have been completed by the study in Wolf *et al* (2020b), where the mechanism of thermo-chemical instability has been proposed to explain the relationship between mode transition and T_g . The present study further supplements this body of work, finding that, for the conditions of relevance, $\Lambda_{ne} \simeq 1.6 \times \Lambda_{777}$ and thus that n_{e0} has been previously overestimated by approximately a factor 1.6. This finding allows to correct the calculations from previous works and should be considered in studies of discharge contraction, a phenomenon that depends on electron-impact ionisation and recombination rates. However, the correction does not affect the conclusions from Wolf *et al* (2019) and Wolf *et al* (2020b) concerning mode transition and ionisation degree.

The study of these contracted discharges has been complemented by the numerical investigations in Groen *et al* (2019) and Viegas *et al* (2020). As mentioned previously, in

Table 5. Summary of the hypotheses listed in section 2.1 and of the results of the numerical and experimental verifications performed in this work.

Nbr	Hypothesis	Verification
1	$I_{777} \simeq \tau_{\text{rad}}^{-1} \frac{n_e n_{\text{O}(2p^4 \text{ } ^3\text{P})} k_{\text{exc}}(T_e)}{\tau_{\text{rad}}^{-1} + n_g k_Q}$	Approximately valid
2	$I_{777} \propto n_e x_{\text{O}} k_{\text{exc}}(T_e)$	$I_{777} \propto \tau_{\text{rad}}^{-1} n_e x_{\text{O}} k_{\text{eff}}(T_e)$
3	E/n_g and k_{exc} radially homogeneous	E/n_g concave and $k_{\text{exc}} \propto n_e$
4	$I_{777} \propto n_e^s$, $1 \leq s \leq 2$	$I_{777} \propto n_e^s$, $1.82 \leq s \leq 2.94$, $s \sim 2.5$
5	x_{O} radially homogeneous	Measured x_{O} concave or homogeneous
6	$I_{777} \propto n_e \propto P_{\text{abs}}$	$I_{777} \propto P_{\text{abs}}^{\text{sp}}$, $1.22 \leq s_p \leq 2.50$, $s_p \sim 2.5$

Groen *et al* (2019) a 3D EM model has simulated the spatial distributions of electric field in these plasmas, given an input profile of n_e . The assumption of $s = 1$ has been used to determine that profile in both the radial and axial directions. For the case of a low-confinement discharge at 100 mbar with a maximum temperature around 4000 K, a $n_e(r)$ profile with similar FWHM as the corrected Λ_{n_e} in condition A in this work (~ 10 mm) but 6 times lower peak, has been considered in Groen *et al* (2019). The resulting radial profiles of E and E/n_g are rather flat for $r < 4$ mm, with values almost twice as much as those reported for condition A in this work (figure 8), and have a convex shape radially outwards. Conversely, in this work, E/n_g has a concave radial profile and E is approximately flat up to $r = 10$ mm. We should notice that different assumptions have been taken on the T_g and n_e profiles and that the method to simulate the electric field is significantly different. While in the plasma reaction–diffusion model of this work $E/n_g(r)$ is found by matching the input $n_e(r)$, in Groen *et al* (2019) E has been found in the whole domain for a given n_e profile by matching the impedance of the plasma with that of the incoming MW field. The model in Groen *et al* (2019) finds E by solving Maxwell’s equations and by assuming power deposition through Ohmic heating and a homogeneous electron-neutral collision frequency. The finding from this work that $\Lambda_{n_e} \simeq 1.6 \times \Lambda_{777}$ means that the profile of n_e should be even broader than that used in Groen *et al* (2019). The adoption of a broader profile of n_e in the model of Groen *et al* (2019) would arguably lead to a broader profile of E , i.e. a profile of E rather flat along a region larger than 4 mm radius. Furthermore, with higher values of n_e , it is predicted that lower values of E would be required to maximise the power transfer to the plasma. Finally, for radial positions beyond the plasma, the different ways of calculating the electric field in the different models determine that $E(r)$ increases with r in Groen *et al* (2019) and decreases with r in this work, which should not be directly compared. Taking these features into account, the profiles of $E(r)$ and $E/n_g(r)$ simulated with the models in Groen *et al* (2019) and in this work are expected to be coherent with each other.

The numerical study in Viegas *et al* (2020) using a zero-dimensional model has also taken n_{e0} as input under the assumption of $s = 1$, mostly in the plasma conditions described in this work as set of conditions C. However, the model in Viegas *et al* (2020) has not directly used any assumption on Λ_{n_e} . We should notice that the correction associated to the interferometry measurements described in section

2.2 would lead most of the n_{e0} values used in Viegas *et al* (2020) (those in hybrid regime and in H-mode) to increase by a factor of approximately 1.5. We have also seen in figure 12 that n_{e0} should be divided by about 1.6, due to the phenomenon of optical contraction. As a result, the two corrections would lead the input values of n_{e0} used in Viegas *et al* (2020) to stay approximately the same. As such, no significant changes are expected in the simulation results and in the conclusions in that paper. Indeed, despite the different models, the values of peak power density simulated in that work are very similar to the corrected $P_{\text{abs}0}$ obtained for the set of conditions C in this work, since the biggest contribution to the calculation of $P_{\text{abs}0}$ is the local collisional term in equation (18). However, in Viegas *et al* (2020), the simulated $P_{\text{abs}0}$ has been compared to the experimentally-estimated one (see figure 3 in Viegas *et al* (2020)). Experimentally, $P_{\text{abs}0}$ in the centre of the plasma has been obtained, as described in Wolf *et al* (2020b), by normalisation of the power density profile to the total power input. This profile has been assumed the same as the one of emission intensity. If, by following the results of this work, 1.6 times higher diameter and length were assumed for the Gaussian profile of P_{abs} , we could expect $P_{\text{abs}0}$ to be $1.6^3 \simeq 4$ times lower. This is a very important difference that appears as the result of the current study. Concerning the comparison of numerical and experimental $P_{\text{abs}0}$ in figure 3 of Viegas *et al* (2020), this correction would explain the discrepancies observed and would lead to a significantly better agreement for pressures below 200 mbar, which increases our confidence in the validity of that model.

The two-dimensional model in Wolf *et al* (2020a), that predicts reactor performances and the mechanisms to obtain them, is also dependent on the spatial profiles of n_e and P_{abs} , as explained in the previous section. As shown in figure 13, the broadening of these profiles leads to a broader high-temperature profile and increased dissociation in the plasma region. However, a more extended temperature profile also leads to slower cooling downstream and thus a broader recombination region. The result of these two effects is higher conversion and energy efficiencies of the simulated reactor at pressures below 140 mbar but lower performances at higher pressures. The broadening of the P_{abs} profile in the flow model and the decrease of its peak also has an influence on the peak of the turbulent viscosity ($\nu_{\text{T,peak}}$ in equation (16)), that is adjusted to match the peak gas temperature with the one measured in Doppler broadening measurements (Wolf *et al* 2019). Indeed, lower $\nu_{\text{T,peak}}$ is obtained, which leads to less gas mixing in

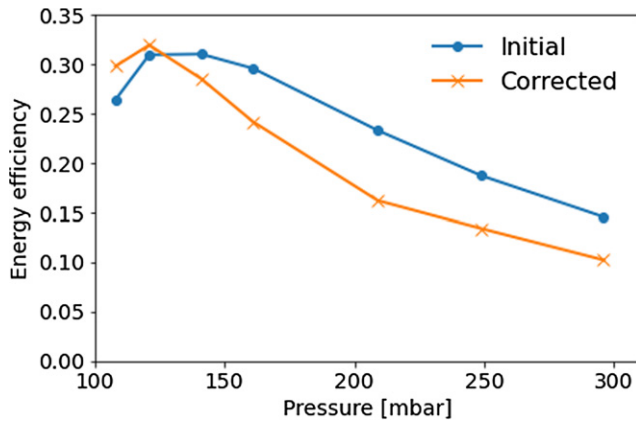


Figure 14. Energy efficiencies as function of pressure, simulated with the flow model in Wolf *et al* (2020a), using the initial assumptions on $n_e(r)$ and $P_{\text{abs}}(r)$ ($\Lambda_{P_{\text{abs}}} = \Lambda_{n_e} = \Lambda_{777}$), and the corrected $n_e(r)$ and $P_{\text{abs}}(r)$ profiles with $\Lambda_{P_{\text{abs}}} \sim \Lambda_{n_e} \sim 1.6 \times \Lambda_{777}$. Results obtained for the set of conditions C.

the simulated domain. However, the broadening of the high-temperature profile allows for dissociation further from the plasma core and thus the negative effect for dissociation of lower gas mixing becomes negligible. The energy efficiencies simulated with the flow model before and after the correction of the spatial profiles are compared in figure 14 for the 7 cases of the set of conditions C. The increase of these efficiencies at lower pressures improves the agreement of the flow simulations with experimental measurements (figure 6 in Wolf *et al* (2020a)), as the broader spatial profiles of P_{abs} and T_g explain the high experimental conversions at low pressure. It is shown that the accurate determination of spatial profiles of discharge parameters should be taken into account when analysing reactor performances. However, for pressures above 140 mbar, the agreement between the flow simulations and the measurements does not improve with the correction. This reinforces the statement in Wolf *et al* (2020a) according to which the energy efficiency at higher pressures depends on the recombination of CO downstream from the plasma, and thus on the neutral chemistry for temperatures below 2000 K.

Although in this section we have focussed on the implications of spatially-resolved plasma parameters for the study of MW contracted discharges for CO₂ conversion, we expect the methods proposed in this work to be relevant for research on other discharges. Firstly, because we have shown that the phenomenon of optical contraction is present not only in atomic plasmas (Golubovskii *et al* 2011, 2020), but also in a molecular gas like CO₂. More generally, we can say that, as spatially-resolved parameters are often difficult to measure, spontaneous optical emission, a natural phenomenon in non-equilibrium plasmas, can provide valuable insight into the spatial distribution of key plasma parameters when interpreted using spatially resolved CRMs. This is particularly the case in plasma sources where the spatial distribution of optical emission is clearly measurable, such as in steady-state DC, RF and MW discharges in cylindrical containers with radii of a few mm or a few cm. Another requirement for the application of the proposed approach is the previous knowledge of line-averaged or

volume-averaged values of electron density or electric field or power density, allowing to take assumptions on their spatial profiles and then correcting them. Other experimental measurements are not required for the application of the methods proposed, although they may be useful as additional model inputs to guarantee that simulations and experiments assess the same conditions. Following the approach we have employed in this work allows to find spatial profiles of different plasma parameters that are important for both understanding and application of discharges.

5. Conclusions

In the present study, a method has been presented to obtain spatially-resolved discharge parameters from emission intensity measurements. Contracted MW discharges for CO₂ conversion at intermediate to high pressures (100–300 mbar) have been addressed, where spatial distributions of the Abel-inverted intensity of the 777 nm line emission ($O(3p^5P) \rightarrow O(3s^5S^0)$), I_{777} , have been measured. Previous experimental studies on these discharges have relied on unverified assumptions on the spatial profiles of discharge parameters, such as electron density (n_e), power density (P_{abs}) and reduced electric field (E/n_g). These profiles have been based on the Gaussian spatial distribution of I_{777} . In this paper, a 1D-radial reaction–diffusion plasma model, including a CRM of atomic oxygen, has been developed and used to resolve discharge parameters in space, by matching the measured I_{777} profiles. It is the first time that such a model has been developed in the context of reactive CO₂ mixtures and used in different conditions of low-confinement and high-confinement discharges. The simulations have allowed us to verify that the experimentally-assumed profile of n_e is not fully consistent with the measurements of the FWHM of I_{777} . Then, they have been used to derive more accurate spatial profiles of n_e , P_{abs} and E/n_g , that have been shown to be consistent with the measurements of I_{777} . Therefore, we have proposed to use this model to obtain accurate radially-resolved discharge parameters from simulations using experimental input.

The numerically-obtained radial profiles of n_e at intermediate to high pressures follow a Gaussian curve with a lower peak than initially assumed and a higher FWHM than the experimentally-observed I_{777} . This phenomenon has been called optical contraction when first reported for atomic plasmas, and has been observed here for the first time in CO₂ MW discharges. According to the simulation results, the optical contraction is mostly justified by a concave profile of E/n_g , resulting from the self-reinforcing cycle of electron-driven collisionality and gas heating in contracted discharges. This leads to an approximately linear relationship between n_e and the electron-impact excitation coefficient of $O(3p^5P)$, the upper state of the 777 nm transition. The optical contraction is also promoted by the concave radial profile of the molar fraction of atomic oxygen in the CO₂ conversion plasma, measured through Raman scattering, that in low-confinement conditions is almost linearly proportional to n_e . The numerically-obtained radial profile of P_{abs} is close to the one of n_e . The relationships between P_{abs} , n_e and I_{777} have been shown to be complex and

dependent on particular conditions. However, we can generally say that for pressures below 150 mbar the FWHM of P_{abs} and n_e are around 1.6 times higher than that of I_{777} . That implies that the peaks of n_e and P_{abs} are, respectively, around 1.6 and $1.6^3 \sim 4$ times lower than previously considered.

Finally, the implications of the proposed corrections to the spatial profiles of discharge parameters on the study of contracted MW discharges for CO₂ conversion have been demonstrated and discussed. The corrections have an impact on our perception of the discharge diameter and of the electric field and power density distributions in the plasma, as well as on our understanding of the main mechanisms determining reactor performances. Indeed, the broader profile of P_{abs} than initially supposed explains the high conversion rates measured for pressures below 140 mbar. Moreover, we have proposed that the procedure developed in this work to determine spatial profiles of discharge parameters can be easily used for the study of plasmas with different configurations and different gases. It has been demonstrated that by combining spatially-resolved numerical simulations with experimental measurements, including measurements of radiative emission intensity, other plasma parameters, such as n_e , P_{abs} and E/n_g , can be retrieved with spatial resolution and replace commonly-used assumptions.

Acknowledgments

The work presented in this paper is part of the European project KEROGREEN, which has received funding from the European Union's Horizon 2020 Research and Innovation Programme under Grant Agreement No. 763909. This work is also part of the Shell-NWO/FOM initiative 'Computational sciences for energy research' of Shell and Chemical Sciences, Earth and Life Sciences, Physical Sciences, FOM and STW. This research has also been carried out under TTW open technology project (Grant No. 15325) in collaboration with Gasunie, Stedin, DNVGL and Ampleon. The work of AvdS received funding from the Netherlands Organization for Scientific Research (NWO) in the framework of the CO₂-to-Products programme with kind support from Shell, and the ENW PPP Fund for the top sectors. We thank Prof. Savino Longo from the University of Bari for discussions on the Monte Carlo Flux method and Prof. Jan van Dijk from the Eindhoven University of Technology for suggestions on fluid modelling. We are also thankful to Tim Righart from DIFFER for gas temperature measurements and to Pieter Willem Groen from DIFFER for discussions on MW power absorption.

Data availability statement

The data that support the findings of this study are available upon reasonable request from the authors.

ORCID iDs

P Viegas  <https://orcid.org/0000-0002-3820-3300>
 L Vialetto  <https://orcid.org/0000-0003-3802-8001>
 A W van de Steeg  <https://orcid.org/0000-0002-2976-7905>
 G J van Rooij  <https://orcid.org/0000-0003-4795-3274>
 M C M van de Sanden  <https://orcid.org/0000-0002-4119-9971>
 P Diomede  <https://orcid.org/0000-0002-4523-3049>
 F J J Peeters  <https://orcid.org/0000-0002-7759-2935>

References

- Alves L L, Bogaerts A, Guerra V and Turner M M 2018 *Plasma Sources Sci. Technol.* **27** 023002
- Alves L L, Coche P, Ridenti M A and Guerra V 2016 *Eur. Phys. J. D* **70** 124
- Annušová A, Marinov D, Booth J P, Sirse N, da Silva M L, Lopez B and Guerra V 2018 *Plasma Sources Sci. Technol.* **27** 045006
- Baeva M, Hempel F, Baierl H, Trautvetter T, Foest R and Loffhagen D 2018 *J. Phys. D: Appl. Phys.* **51** 385202
- Barklem P S 2007 *Astron. Astrophys.* **462** 781–8
- Bongers W et al 2017 *Plasma Process. Polym.* **14** e1600126
- Butylkin Y P, Zhivotov V K, Krasheninnikov E G, Krotov M F, Rusanov V D, Tarasov Y V and Fridman A A 1981 *Sov. Phys. - Tech. Phys.* **26** 555–8
- Capitelli M, Bruno D and Laricchiuta A 2013 *Fundamental Aspects of Plasma Chemical Physics: Transport* (New York: Springer)
- Capitelli M, Celiberto R, Colonna G, Esposito F, Gorse C, Hassouni K, Laricchiuta A and Longo S 2015 *Fundamental Aspects of Plasma Chemical Physics: Kinetics* vol 85 (Springer)
- Caplinger J E and Perram G P 2020 *Plasma Sources Sci. Technol.* **29** 015011
- Carbone E A D, Hübner S, Palomares J M and van der Mullen J J A M 2012 *J. Phys. D: Appl. Phys.* **45** 345203
- D'Isa F A, Carbone E A D, Hecimovic A and Fantz U 2020 *Plasma Sources Sci. Technol.* **29** 105009
- Dagdigan P J, Forch B E and Miziolek A W 1988 *Chem. Phys. Lett.* **148** 299–308
- den Harder N et al 2017 *Plasma Process. Polym.* **14** e1600120
- Durandet A, Arnal Y, Margot-Chaker J and Moisan M 1989 *J. Phys. D: Appl. Phys.* **22** 1288
- Dyatko N A, Ionikh Y Z, Kochetov I V, Marinov D L, Meshchanov A V, Napartovich A P, Petrov F B and Starostin S A 2008 *J. Phys. D: Appl. Phys.* **41** 055204
- Eliasson B and Kogelschatz U 1986 *J. Phys. B: At. Mol. Phys.* **19** 1241–7
- Erdman P W and Zipf E C 1987 *J. Chem. Phys.* **87** 4540
- Fiebrandt M, Bibinov N and Awakowicz P 2020 *Plasma Sources Sci. Technol.* **29** 045018
- Fiebrandt M, Hillebrand B, Spiekermeier S, Bibinov N, Böke M and Awakowicz P 2017 *J. Phys. D: Appl. Phys.* **50** 355202
- Fleisch T, Kabouzi Y, Moisan M, Pollak J, Castañón-Martínez E, Nowakowska H and Zakrzewski Z 2007 *Plasma Sources Sci. Technol.* **16** 173–82
- Fridman A 2008 *Plasma Chemistry* (Cambridge: Cambridge University Press)
- Fridman A and Kennedy L A 2004 *Plasma Physics and Engineering* (London: Taylor and Francis)
- Georgieva V et al 2017 *Plasma Process. Polym.* **14** 1600185
- Giovangigli V 1990 *Impact Comput. Sci. Eng.* **2** 73–97
- Goede A P H, Bongers W A, Graswinckel M F, van de Sanden R M C M, Leins M, Kopecki J, Schulz A and Walker M 2014 *EPJ Web Conf.* **79** 01005

- Golubovskii Y B, Kalanov D and Maiorov V 2017 *Phys. Rev. E* **96** 023206
- Golubovskii Y B, Nekuchaev V, Gorchakov S and Uhrlandt D 2011 *Plasma Sources Sci. Technol.* **20** 053002
- Golubovskii Y B, Siasko A V and Nekuchaev V O 2020 *Plasma Sources Sci. Technol.* **29** 065020
- Gordiets B F, Ferreira C M, Guerra V L, Loureiro J M A H, Nahorny J, Pagnon D, Touzeau M and Vialle M 1995 *IEEE Trans. Plasma Sci.* **23** 750–68
- Gregório J, Boisse-Laporte C and Alves L L 2010 *Eur. Phys. J. Appl. Phys.* **49** 13102
- Gregório J, Leprince P, Boisse-Laporte C and Alves L L 2012 *Plasma Sources Sci. Technol.* **21** 015013
- Groen P W C, Wolf A J, Righart T W H, van de Sanden M C M, Peeters F J J and Bongers W A 2019 *Plasma Sources Sci. Technol.* **28** 075016
- Grofulović M, Alves L L and Guerra V 2016 *J. Phys. D: Appl. Phys.* **49** 395207
- Guerra V, Silva T, Ogloblina P, Grofulović M, Terraz L, da Silva M L, Pintassilgo C D, Alves L L and Guaitella O 2017 *Plasma Sources Sci. Technol.* **26** 11LT01
- Hirschfelder J O and Curtiss C F 1949 Flame propagation in explosive gas mixtures *3rd Symp. on Combustion, Flame and Explosion Phenomena* pp 121–7
- Ikegami H 1968 *Japan. J. Appl. Phys.* **7** 634–55
- Itikawa Y 2009 *J. Phys. Chem. Ref. Data* **38** 1
- Jimenez-Diaz M, Carbone E A D, van Dijk J and van der Mullen J J A M 2012 *J. Phys. D: Appl. Phys.* **45** 335204
- Kabouzi Y, Graves D B, Martinez E C and Moisan M 2007 *Phys. Rev. E* **75** 016402
- Kanik I, Noren C, Makarov O P, Vattipalle P, Ajello J M and Shemansky D E 2003 *J. Geophys. Res.* **108** 5126
- Koelman P, Heijkers S, Tadayon Mousavi S, Graef W, Mihailova D, Kozák T, Bogaerts A and van Dijk J 2017 *Plasma Process. Polym.* **14** 1600155
- Kossyi I A, Kostinsky A Y, Matveyev A A and Silakov V P 1992 *Plasma Sources Sci. Technol.* **1** 207–20
- Kozák T and Bogaerts A 2014 *Plasma Sources Sci. Technol.* **23** 045004
- Kramida A, Ralchenko Y, Reader J and Team N A 2020 *NIST Standard Reference Database 78—Atomic Spectra Database (Ver. 5.8)* Gaithersburg National Institute of Standards and Technology
- Laher R R and Gilmore F R 1990 *J. Phys. Chem. Ref. Data* **19** 277
- Laricchiuta A et al 2009 *Eur. Phys. J. D* **54** 607–12
- Lawrence G M 1970 *Phys. Rev. A* **2** 387–407
- Lieberman M A and Lichtenberg A J 2005 *Principles of Plasma Discharges and Materials Processing* (New York: Wiley)
- Martinez E C, Kabouzi Y, Makasheva K and Moisan M 2004 *Phys. Rev. E* **70** 066405
- McConkey J W, Malone C P, Johnson P V, Winstead C, McKoy V and Kanik I 2008 *Phys. Rep.* **466** 1–103
- Mewe R 1967 *Br. J. Appl. Phys.* **18** 107–18
- Moisan M and Pelletier J 2012 *Physics of Collisional Plasmas: Introduction to High-Frequency Discharges* (Springer)
- Mori T, Kanou K, Mizuta K, Kuramasu T, Ishikawa Y and Arai S 1992 *J. Chem. Phys.* **97** 9094
- Morillo-Candas A S, Drag C, Booth J-P, Dias T C, Guerra V and Guaitella O 2019 *Plasma Sources Sci. Technol.* **28** 075010
- Mousavi S T, Carbone E, Wolf A, Bongers W and van Dijk J 2021 Two-temperature balance equations implementation, numerical validation and application to H₂O-He microwave induced plasmas <https://doi.org/10.1088/1361-6595/ac0a44>
- Niemi K, von der Gathen V S and Döbele H F 2001 *J. Phys. D: Appl. Phys.* **34** 2330–5
- Parker J V 1963 *Phys. Fluids* **6** 1657–8
- Patankar S V 1980 *Numerical Heat Transfer and Fluid Flow* (London: Taylor and Francis)
- Petrov G M and Ferreira C M 1999 *Phys. Rev. E* **59** 3571–82
- Pietanza L D, Colonna G and Capitelli M 2020 *Plasma Sources Sci. Technol.* **29** 035022
- Ridenti M A, Amorim J D, Pino A D, Guerra V and Petrov G 2018 *Phys. Rev. E* **97** 013201
- Santos M, Noël C, Belmonte T and Alves L L 2014 *J. Phys. D: Appl. Phys.* **47** 265201
- Schaefer G and Hui P 1990 *J. Comput. Phys.* **89** 1–30
- Schottky W 1924 *Phys. Z.* **25** 342
- Shneider M N, Mokrov M S and Milikh G M 2014 *Phys. Plasmas* **21** 032122
- Silva A F, Morillo-Candas A S, Tejero-del-Caz A, Alves L L, Guaitella O and Guerra V 2020 *Plasma Sources Sci. Technol.* **29** 125020
- Smith G P et al 2018 *GRI-MECH 3.0 database* <http://combustion.berkeley.edu/gri-mech/version30/text30.html>
- Snoeckx R and Bogaerts A 2017 *Chem. Soc. Rev.* **46** 5805–63
- Stancu G D, Leroy O, Coche P, Gadonna K, Guerra V, Minea T and Alves L L 2016 *J. Phys. D: Appl. Phys.* **49** 435202
- Sushkov V P, Do H T and Hippler R 2013 *Contrib. Plasma Phys.* **53** 549–59
- Synek P, Obrusník A, Hübner S, Nijdam S and Zajčková L 2015 *Plasma Sources Sci. Technol.* **24** 025030
- van de Steeg A W, Butterworth T, van den Bekerom D C M, Silva A F, van de Sanden M C M and van Rooij G J 2020 *Plasma Sources Sci. Technol.* **29** 115001
- van de Steeg A W, Vialetto L, Silva A F, Peeters F J J, van den Bekerom D C M, Gatti N, Diomede P, van de Sanden M C M and van Rooij G J 2021 *Opt. Lett.* **46** 2172–5
- van den Bekerom D C M, Linares J M P, Verreycken T, van Veldhuizen E M, Nijdam S, Berden G, Bongers W A, van de Sanden M C M and van Rooij G J 2019 *Plasma Sources Sci. Technol.* **28** 055015
- van den Bekerom D C M, van de Steeg A, van de Sanden M C M and van Rooij G J 2020 *J. Phys. D: Appl. Phys.* **53** 054002
- van Gessel A F H, Carbone E A D, Bruggeman P J and van der Mullen J J A M 2012 *Plasma Sources Sci. Technol.* **21** 015003
- van Rooij G J et al 2015 *Faraday Discuss.* **183** 233–48
- Vermeiren V and Bogaerts A 2020 *J. Phys. Chem. C* **124** 18401–15
- Vialetto L, Longo S and Diomede P 2019 *Plasma Sources Sci. Technol.* **28** 115015
- Vialetto L, Viegas P, Longo S and Diomede P 2020 *Plasma Sources Sci. Technol.* **29** 115006
- Viegas P, Vialetto L, Wolf A J, Peeters F J J, Groen P W C, Righart T W H, Bongers W A, van de Sanden M C M and Diomede P 2020 *Plasma Sources Sci. Technol.* **29** 105014
- Wolf A J, Peeters F J J, Groen P W C, Bongers W A and van de Sanden M C M 2020a *J. Phys. Chem. C* **124** 16806–19
- Wolf A J, Righart T W H, Peeters F J J, Bongers W A and van de Sanden M C M 2020b *Plasma Sources Sci. Technol.* **29** 025005
- Wolf A J, Righart T W H, Peeters F J J, Groen P W C, van de Sanden M C M and Bongers W A 2019 *Plasma Sources Sci. Technol.* **28** 115022
- Yimer I, Campbell I and Jiang L-Y 2002 *Can. Aeronaut. Space J.* **48** 195–200
- Zhong H, Shneider M N, Mokrov M S and Ju Y 2019 *J. Phys. D: Appl. Phys.* **52** 484001